

## The design and performance of the *Gaia* photometric system

C. Jordi,<sup>1,2\*</sup> E. Høg,<sup>3</sup> A. G. A. Brown,<sup>4</sup> L. Lindegren,<sup>5</sup> C. A. L. Bailer-Jones,<sup>6</sup> J. M. Carrasco,<sup>1</sup> J. Knude,<sup>3</sup> V. Straižys,<sup>8</sup> J. H. J. de Bruijne,<sup>10</sup> J.-F. Claeskens,<sup>11</sup> R. Drimmel,<sup>12</sup> F. Figueras,<sup>1,2</sup> M. Grenon,<sup>7</sup> I. Kolka,<sup>13</sup> M. A. C. Perryman,<sup>10</sup> G. Tautvaišienė,<sup>8</sup> V. Vansevicius,<sup>9</sup> P. G. Willemsen,<sup>14</sup> A. Bridžius,<sup>9</sup> D. W. Evans,<sup>15</sup> C. Fabricius,<sup>1,2,3</sup> M. Fiorucci,<sup>17</sup> U. Heiter,<sup>16</sup> T. A. Kaempf,<sup>14</sup> A. Kazlauskas,<sup>8</sup> A. Kučinskas,<sup>5,8</sup> V. Malyuto,<sup>13</sup> U. Munari,<sup>17</sup> C. Reylé,<sup>18</sup> J. Torra,<sup>1,2</sup> A. Vallenari,<sup>19</sup> K. Zdanavičius,<sup>8</sup> R. Korakitis,<sup>20</sup> O. Malkov<sup>21</sup> and A. Smette<sup>22</sup>

<sup>1</sup>Department Astronomia i Meteorologia, Universitat de Barcelona, Avda. Diagonal, 647, E-08028 Barcelona, Spain

<sup>2</sup>Institut d'Estudis Espacials de Catalunya (IEEC), Edif.Nexus, C/Gran Capità, 2-4, 08034 Barcelona, Spain

<sup>3</sup>Niels Bohr Institute, Juliane Maries Vej 32, DK-2100, Copenhagen Ø, Denmark

<sup>4</sup>Sterrewacht Leiden, PO Box 9513, 2300 RA Leiden, the Netherlands

<sup>5</sup>Lund Observatory, Lund University, Box 43, 221 00 Lund, Sweden

<sup>6</sup>Max-Planck-Institut für Astronomie, Königstuhl 17, 69117 Heidelberg, Germany

<sup>7</sup>Observatoire de Genève, Chemin des Maillettes 51, CH-1290 Sauverny, Switzerland

<sup>8</sup>Institute of Theoretical Physics and Astronomy, Vilnius University, Goštauto 12, Vilnius LT-01108, Lithuania

<sup>9</sup>Institute of Physics, Savanoriu 231, LT-02300 Vilnius, Lithuania

<sup>10</sup>ESA/ESTEC, Research and Scientific Support Department, PO Box 299, 2200 AG Noordwijk, the Netherlands

<sup>11</sup>Institut d'Astrophysique et de Géophysique, Université de Liège, Allée du 6 Août 17, B-4000 Sart Tilman (Liège), Belgium

<sup>12</sup>INAF – Osservatorio Astronomico di Torino, Strada Osservatorio 20, I-10025 Pino Torinese, Italy

<sup>13</sup>Tartu Observatory, 61602 Tõravere, Estonia

<sup>14</sup>Sternwarte der Universität Bonn, Auf dem Hügel 71, 53121 Bonn, Germany

<sup>15</sup>Institute of Astronomy, Madingley Road, Cambridge, CB3 0HA

<sup>16</sup>Department of Astronomy and Space Physics, Uppsala University, Box 515, SE-75120 Uppsala, Sweden

<sup>17</sup>INAF – Osservatorio Astronomico di Padova, Sede di Asiago, 36012 Asiago (VI), Italy

<sup>18</sup>CNRS-UMR6091, Observatoire de Besançon, BP 1615, F-25010 Besançon, France

<sup>19</sup>INAF – Osservatorio di Padova, Vicolo Osservatorio 5, 35122 Padova, Italy

<sup>20</sup>Dionysos Satellite Observatory, National Technical University of Athens, Heroon Polytechniou 9, GR-15780 Zografos, Greece

<sup>21</sup>Institute of Astronomy, 48 Pyatnitskaya St. 119017 Moscow, Russia

<sup>22</sup>European Southern Observatory, Casilla 19001, Alonso de Cordova 3107, Vitacura, Santiago, Chile

Accepted 2005 December 1. Received 2005 November 30; in original form 2005 November 18

### ABSTRACT

The European *Gaia* astrometry mission is due for launch in 2011. *Gaia* will rely on the proven principles of the ESA *Hipparcos* mission to create an all-sky survey of about one billion stars throughout our Galaxy and beyond, by observing all objects down to 20 mag. Through its massive measurement of stellar distances, motions and multicolour photometry, it will provide fundamental data necessary for unravelling the structure, formation and evolution of the Galaxy. This paper presents the design and performance of the broad- and medium-band set of photometric filters adopted as the baseline for *Gaia*. The 19 selected passbands (extending from the UV to the far-red), the criteria and the methodology on which this choice has been based are discussed in detail. We analyse the photometric capabilities for characterizing the luminosity, temperature, gravity and chemical composition of stars. We also discuss the automatic determination of these physical parameters for the large number of observations involved, for objects located throughout the entire Hertzsprung–Russell diagram. Finally, the capability of the photometric system (PS) to deal with the main *Gaia* science case is outlined.

\*E-mail: carme@am.ub.es

**Key words:** instrumentation: photometers – space vehicles: instruments – techniques: photometric – stars: fundamental parameters – Galaxy: formation – Galaxy: structure.

## 1 INTRODUCTION

*Gaia* has been approved as a cornerstone mission in the ESA scientific programme. The main goal is to provide data to study the formation and subsequent dynamical, chemical and star formation evolution of the Milky Way galaxy (Perryman et al. 2001; Mignard 2005). *Gaia* will achieve this by providing an all-sky astrometric and photometric survey complete to 20 mag in unfiltered light. During the mission, on-board object detection will be employed and more than 1 billion stars will be observed (as well as non-stellar objects to similar completeness limits). The full-mission (5-yr) mean-sky parallax accuracies are expected to be around 7 microarcsec (7  $\mu$ as) at  $V = 10$ , 12–25  $\mu$ as at  $V = 15$  and 100–300  $\mu$ as at  $V = 20$  (depending on spectral type). Multi-epoch, multicolour photometry covering the optical wavelength range will reach the same completeness limit. Radial velocities will be obtained for 100–150 million stars brighter than  $V \simeq 17$ –18 mag with accuracies of around 1–15 km s<sup>-1</sup>, depending on the apparent magnitude and spectral type of the stars and the sky density (for details see Katz et al. 2004; Wilkinson et al. 2005).

The photometric measurements provide the basic diagnostics for classifying all objects as stars, quasars, Solar system objects, or otherwise and for parametrizing them according to their nature. Stellar classification and parametrization across the entire Hertzsprung–Russell (HR) diagram is required as well as the identification of peculiar objects. This demands observation in a wide wavelength range, extending from the UV to the far-red. The photometric data must determine:

- (i) effective temperatures and reddening at least for O–B–A stars (needed both as tracers of Galactic spiral arms and as reddening probes);
- (ii) at least effective temperatures and abundances for F–G–K–M giants and dwarfs;
- (iii) luminosities (gravities) for stars having large relative parallax errors;
- (iv) indications of unresolved multiplicity and peculiarity; and
- (v) a map of the interstellar extinction in the Galaxy.

All of this has to be done with an accuracy sufficient for stellar age determination in order to allow for a quantitative description of the chemical and dynamical evolution of the Galaxy over all galactocentric distances. Separate determination of Fe- and  $\alpha$ -element abundances is essential for mapping Galactic chemical evolution and understanding the formation of the Galaxy.

Photometry is also crucial to identify and characterize the set of  $\sim 500\,000$  quasars that the mission will detect. Apart from being astrophysically interesting in their own right, quasars are key objects for defining the fixed, non-rotating *Gaia* Celestial Reference Frame, the optical equivalent of the International Celestial Reference Frame (Mignard 2005). On the other hand, *Gaia* will identify about 900 quasars with multiple images produced by macrolensing. Because this number is sensitive to cosmological parameters, the *Gaia* observations will be able to constrain the latter.

Due to diffraction and the optical aberrations of the instrument, the position of the centre of the stellar images is wavelength dependent. To achieve the microarcsec accuracy level, astrometry has to be corrected for this chromatic aberration through the knowledge of the spectral energy distribution (SED) of the observed objects. Photometry is indispensable for this. If uncorrected, chromatic errors could reach several milliarcsec, cf. Section 5.1.2.

As explained in the following sections, the photometric systems (PSs) proposed during the long development of *Gaia* have been improved along with the increasing collecting area of the telescopes, with better insight into the astrophysical requirements, and with the development of mathematical tools to compare the various proposed systems. The use of charge-coupled devices (CCDs) in a scanning astrometry satellite was first proposed in 1992 (Høg 1993) as the *ROEMER* project. The proposal included five broad passbands, *UBVRI*, which would obtain much better precision than the *B, V* of *Hipparcos-Tycho* although with a similar collecting aperture. The *Gaia* collecting area has increased by up to 10 times with respect to *ROEMER* and, consequently, the initial PS has been upgraded several times. Eight medium-width passbands were proposed by Straižys & Høg (1995) and spectrophotometry instead of filter photometry was also considered in Høg (1998). A system of four broad and 11 medium-width passbands was proposed by Grenon et al. (1999) and adopted in the ‘*Gaia* Study Report’ (ESA 2000).<sup>1</sup> The subsequent developments and updates have yielded the present baseline with five broad- and 14 medium-width passbands.

This paper deals with the definition of the PS, the relationship of its passbands with the stellar astrophysical diagnostics and the evaluation of its performance in terms of the astrophysical parametrization of single stars. This is based on the specific design implementation of the payload commonly referred to as *Gaia-2* (cf. Section 2) applicable at the end of the technology assessment phase as of mid-2005. The resulting astrometric and photometric requirements form the basis of the industrial specifications for the satellite implementation phase, with the consequence that the detailed design, due for finalization early in 2007, may differ in detail from the present description. Nevertheless, the principles and objectives as well as the methods and assessment tools described in this paper will remain applicable.

The paper is organized as follows. Section 2 describes the mission observation strategy, telescopes and focal planes. Section 3 deals with the measurement of the unfiltered light in the fields of view. The principles of designing the multicolour PS are outlined in Section 4, and the purpose of the broad- and medium-passbands is discussed in detail in Section 5. Synthetic photometry and corresponding error estimates are given in Section 6. The performance of the PS with respect to astrophysical parameter (AP) determination is quantified in Section 7. In Section 8, the potential of the PS for Galactic structure and evolution studies as well as the performances for quasi-stellar objects (QSOs) are outlined. Finally, Section 9 and Appendix A present the conclusions and describe the ‘Figure of

<sup>1</sup> The *Gaia* technical reports are available from the *Gaia* Photometry Working Group website: <http://gaia.am.ub.es/PWG/documents/MNRAS/>

**Table 1.** *Gaia*-2 characteristics of the Astro and Spectro instruments.

Instrument		Astro	Spectro	
Photometer		Broad-band	Medium-band (blue)	Medium-band (red)
$F$	Focal length (m)	46.7	2.3	2.3
$A$	Telescope pupil area (m <sup>2</sup> )	$1.4 \times 0.5 = 0.7$	$0.5 \times 0.5 = 0.25$	$0.5 \times 0.5 = 0.25$
$n_{\text{sup}}$	Number of superimposed fields	2	1	1
$T_0(\lambda)$	Telescope transmittance <sup>a</sup>	$T_{\text{Ag}}^6(\lambda)$	$0.8 \times T_{\text{Al}}^3(\lambda)$	$T_{\text{Al}}^3(\lambda)$
$\tau$	Integration time (s) per single CCD	3.31	12.0	12.0
$Q(\lambda)$	CCD quantum efficiency	CCD-green	CCD-blue	CCD-red
$r$	Total detection noise (e <sup>-</sup> sample <sup>-1</sup> )	6.6	7.3	7.3
	Available number of filter strips	4 (10 rows)	10 (2 rows)	6 (2 rows)
	Field of view across scan (deg)	0.7236	1.4685	1.4685
$n_{\text{obs}}$	Mean number of observations per strip (5 yr) <sup>b</sup>	83	84	84
	Sample size on sky (arcsec × arcsec) <sup>c</sup>	$0.0442 \times 1.5912$	$0.897 \times 1.346$	$0.897 \times 1.346$
	Double-star resolution (arcsec)	0.05–0.1	0.5–1	0.5–1
	No-filter magnitude	$G$	–	$GS$

<sup>a</sup> $T_X^n(\lambda)$  denotes  $n$  reflections of material X. The factor 0.8 in MBP-blue comes from the dichroic beam splitter. <sup>b</sup>The number of observations with Astro ranges from  $\sim 40$  to 250 and in Spectro from  $\sim 50$  to 220. <sup>c</sup>Sample size on the sky: a sample is a binning of CCD pixels in an area along-scan × across-scan.

Merit' (FoM) mathematical tool for the comparison of filter systems, respectively.

Throughout the rest of the paper, we will use the following abbreviations: AP, astrophysical parameter; BBP, broad-band photometer; C1B, set of passbands implemented in the Astro instrument; C1M, set of passbands implemented in the Spectro instrument; CCD, charge coupled device; FoM, figure of merit; MBP, medium-band photometer; MDM, minimum distance method; NN, neural network; PS, photometric system; QE, CCD quantum efficiency; QSO, quasar; SED, spectral energy distribution; S/N, signal-to-noise ratio; and ST, scientific target.

## 2 INSTRUMENT DESCRIPTION

### 2.1 Observation strategy

*Gaia* is a survey mission. Operating from a Lissajous orbit around the second Lagrange point of the Sun–Earth/Moon system (L2), the satellite will continuously observe the sky. During its 5-yr mission, *Gaia* will rotate, at a fixed speed of 60 arcsec s<sup>-1</sup>, around a slowly precessing spin axis. As a result of this spin motion, objects traverse the focal planes, which have viewing directions oriented at right angles to the spin axis. The along-scan direction is defined as the direction in which the images move in the focal plane and the across-scan direction is defined as the perpendicular direction. Thus, an object crosses the field of view in the along-scan direction at a roughly constant across-scan coordinate.

*Gaia* observations are made with high-quality, large-format CCDs. These detectors are operated in time delay and integration mode, with charge images being transported (clocked) in synchrony with optical images moving across the field due to the rotation of the satellite. In principle, each CCD may be equipped with a filter (an interference, standard coloured glass or multilayer filter) defining, together with the telescope transmission and the CCD quantum efficiency (QE), a certain photometric passband. By design, the arrangement of CCDs and filters in the focal planes ensures redundancy in case of failure.

Stars brighter than  $\sim 12$  mag pose a special challenge. Pixel saturation may be avoided for such objects by the activation of gates on the CCD, effectively reducing the CCD integration time.

### 2.2 *Gaia* instruments

*Gaia* will perform measurements by means of two physically distinct instruments, with different viewing directions: the Astro instrument, designed for astrometric and broad-band photometric observations; and the Spectro instrument, used for medium-band photometry and radial-velocity measurements. Astro and Spectro differ in spatial resolution, available integration time, the number and type of passbands that can be used, and in telescope transmission and detector characteristics (Table 1 and Fig. 1).

The astrometric focal plane incorporates three functions: (i) the sky mapper; (ii) the main astrometric field; and (iii) the broad-band photometer (BBP; Section 5.1). Broad-band photometry is mainly aimed at sampling the SED of objects over a wide wavelength range to allow on-ground correction of image centroids measured in the main astrometric field for systematic chromatic shifts caused by aberrations. In addition, BBP measurements contribute to the astrophysical characterization of objects, especially in dense stellar fields.

Through implementation of a dichroic beam splitter, the Spectro instrument serves two distinct focal planes: one for the radial-velocity spectrometer (RVS), and one for the medium-band photometer (MBP; Section 5.2). The Spectro/MBP focal plane incorporates two functions: (i) a sky mapper; and (ii) the MBP instrument. The main goal of medium-band photometry is to determine the APs of objects, which, in combination with the astrometric measurements, will enable astronomers to fulfil the main science objective of *Gaia*. RVS observes a spectral region around 860 nm at a nominal resolution of 11 500. Its main aim is to determine radial velocities for bright stars, down to  $V \simeq 17$ –18 mag. For the brightest ones, astrophysical parametrization is also foreseen.

The angular resolution of the instruments allows photometry to be obtained at stellar densities up to 750 000 stars deg<sup>-2</sup> in the BBP and up to 200 000–400 000 stars deg<sup>-2</sup> in the MBP (cf. Section 6.3). The resolution limit for double stars is about 0.05–0.1 arcsec in the Astro field and 0.5–1 arcsec in the MBP.

### 2.3 Sky mappers

Both sky mappers work in unfiltered light and allow autonomous object detection and confirmation, including rejection of prompt

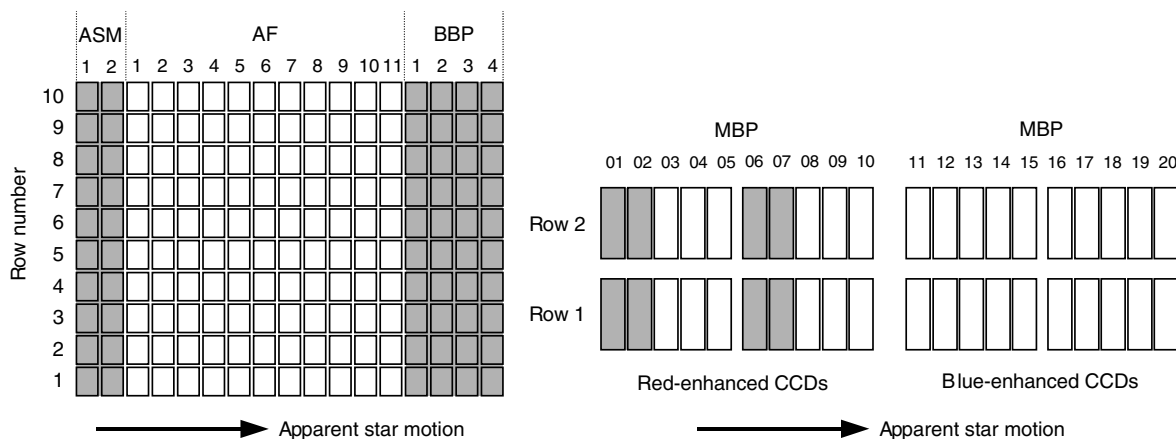


**Figure 1.** Schematic layout for the Astro field (left) and the Spectro/MBP field (right) in *Gaia*-2. The designations BBP1–BBP4 and MBP01–MBP20 refer to the physical locations of the CCDs in the along-scan direction within the field, independent of their functionality (e.g. for detection or photometry) and the assignment of filters between them. The Spectro sky mapper, operating without filters, is physically located at MBP01, 02, 06, and 07. ASM and AF are the Astro sky mapper and the Astro field, respectively.

particle events (cosmic rays, solar protons, etc.). Detection and confirmation probabilities are a function of magnitude and object density in the field of view. They are effectively unity up to the survey limit (20 mag) dropping quickly to zero for fainter objects (Arenou et al. 2005). On-board object detection has several advantages:

- (i) sampling of detected objects can be limited to ‘windows’, i.e. areas centred on the object (Høg 2005), which allows to flush useless pixels containing empty sky, which is of benefit to both CCD readout noise and the data volume to be transmitted to ground;
- (ii) it allows the unbiased detection of all objects, assuring that the resulting catalogue will be complete to the survey limit; and
- (iii) unpredictable ‘peculiar objects’, such as supernovae or Solar system objects, will be observed, if brighter than the detection limit.

Moreover, on-board detection is mandatory as no input catalogue exists that is complete to the survey limit at the *Gaia* spatial resolution.

## 2.4 Astro/broad-band photometer

*Gaia* astrometric observations are made without a filter in order to minimize photon noise. The mirror coatings and CCD QE effectively define a broad (white-light) passband, called *G* (Section 3). The Astro focal plane receives the light from the superposition of two viewing directions on the sky, separated by the so-called ‘basic angle’, of order  $100^\circ$ . This superposition of the two fields of view will lead to a number of complications in the data processing, but throughout this paper we only consider the first-order effect of the doubling of the diffuse sky-background.

The BBP consists of 40 CCDs, arranged in four across-scan strips and 10 along-scan rows (the *Gaia* naming convention for the along-scan direction is rows of CCDs and columns of CCD pixels, and across-scan we speak of strips of CCDs and lines of pixels). In principle, the filters can be distributed among the 40 CCDs in any combination that is desirable from a scientific point of view. A preferable situation, for example for variable-star science, would be to have identical filters on each of the 10 CCD rows within a single CCD strip: this would yield quasi-simultaneous measurements in the different passbands on each field-of-view crossing, independent of the across-scan coordinate of an object. However, such a solution would

limit the number of BBP passbands to the number of CCD strips, i.e. four.

## 2.5 Spectro/medium-band photometer

The MBP consists of 40 CCDs arranged in 20 strips and two rows. The CCDs in the first 10 strips are illuminated directly from the Spectro telescope. These CCDs are red enhanced, which means they are thicker than ‘normal CCDs’ and have a red-optimized antireflection coating. The CCDs in the last 10 strips receive only the blue light from the Spectro telescope. These detectors are blue enhanced, which means they have the same thickness as ‘normal CCDs’ but a blue-optimized antireflection coating. Four of the red-enhanced strips act as sky mappers and do not have filters; the associated broad passband is called *GS*. The remaining six strips with red- and the 10 strips with blue-enhanced CCDs may be equipped with filters, defining up to 16 different passbands, assuming the two CCD rows in each strip have identical filters (for the sake of redundancy). One of the red passbands will cover the same spectral region as the RVS, around 860 nm, leaving 15 free strips.

## 3 THE *G* AND *GS* PASSBANDS

The *G* and *GS* passbands corresponding to the white light observations in the Astro and Spectro instruments, respectively, are shown in Fig. 2. They cover the wavelength range from 400 to 1000 nm and 350 to 1025 nm, with the maximum energy transmission at  $\sim 715$  and  $\sim 765$  nm and the FWHM of 408 and 456 nm, respectively for *G* and *GS*. The relation between the associated magnitudes and the Johnson *V* magnitude is shown in Fig. 3. Very red objects (either intrinsically red or highly reddened) are much brighter in *G* and *GS* than in *V* and, therefore, the *Gaia* limiting magnitude of  $G_{\text{lim}} \sim 20$  translates into  $V_{\text{lim}} \sim 20\text{--}25$ , depending on the colour of the observed object.

The estimated precisions for the *G* magnitudes per focal plane transit and at the end of the mission, computed as described in Section 6.2, are shown in Fig. 4. Taking into account the photon noise from the source, the background and the readout noise, precisions of  $\sim 10$  and  $\sim 1$  mmag are achievable at  $V \sim 19$ . This implies that the precision of the *G* measurements is ultimately limited by the calibration errors (see Section 6.4).

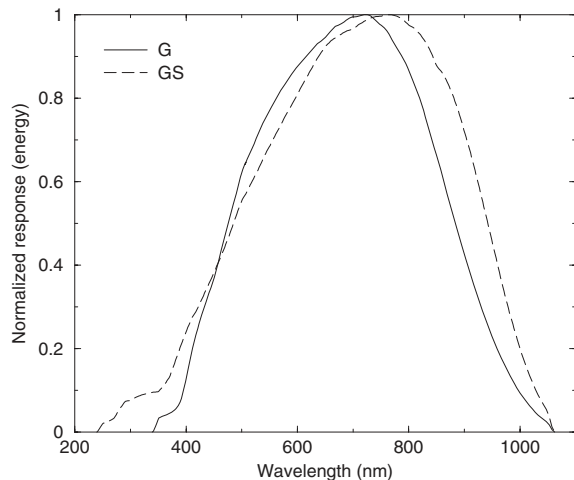


**Figure 2.** The *G* and *GS* *Gaia* broad passbands corresponding to the white light observations in the Astro and Spectro focal planes, respectively.

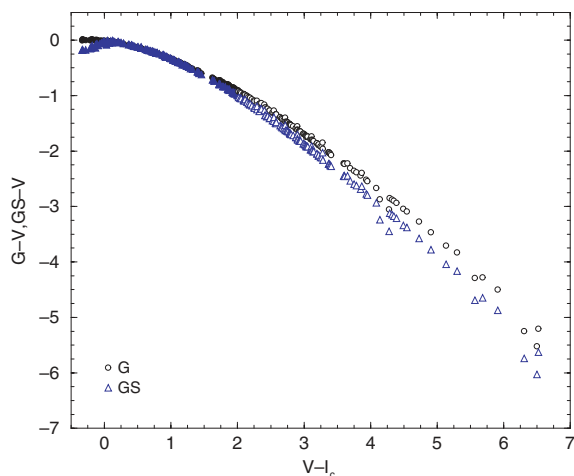


**Figure 3.** The relation between  $G - V$  and  $GS - V$  and  $V - I_C$  for the white light passbands in the Astro and Spectro focal planes. Every star in the spectral library of Pickles (1998) is represented by a filled symbol. Open symbols correspond to the same stars reddened by  $A_V = 5$  mag. Reddening vectors run parallel to the colour–colour relationship. Pickles’ library was chosen because it extends to very red objects. No appreciable differences for stars with  $T_{\text{eff}} \geq 4000$  K are obtained when using spectral energy distributions from the BaSeL 2.2 library or other libraries.

*Gaia* will provide distances at the 10 per cent accuracy level for some 100–200 million stars, which, combined with estimates of the *G* magnitude and the interstellar extinction, will yield unprecedented absolute magnitudes, in both accuracy and number.

The *G* passband also yields the best signal-to-noise ratio (S/N) for variability detection among all the *Gaia* passbands. *Gaia* will monitor millions of variable stars (eclipsing binaries, Cepheids, RR Lyrae, Mira-LPVs, etc.). Eyer (2005) and Eyer & Mignard (2005) provide comparisons with other variability surveys and a detailed discussion of the effects of the variable time sampling and number of observations due to the scanning law.

#### 4 DESIGNING THE PHOTOMETRIC SYSTEM

Many ground-based PSs exist but none satisfies all the requirements of a space-based mission such as *Gaia*: portions of the spectrum

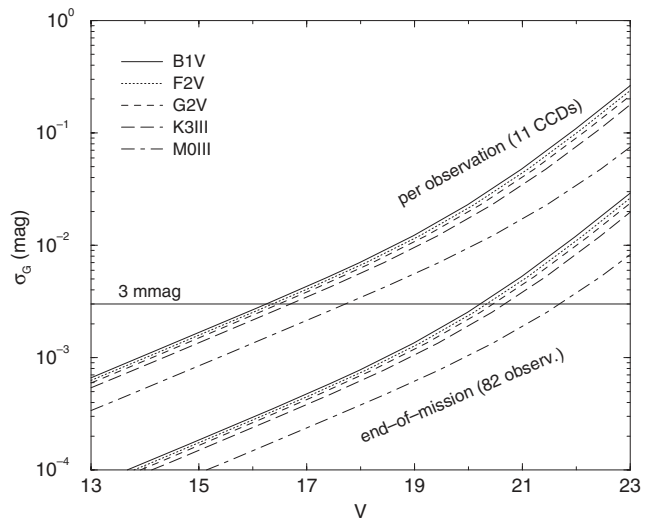


**Figure 4.** Estimated precision of the *G* magnitude per focal plane transit and at the end of the mission according to equation (2) assuming  $\sigma_{\text{cal}} = 0$ . In this paper, the contribution of calibration error to the end-of-mission precision is assumed to be 3 mmag (horizontal line).

limited on-ground by telluric  $\text{O}_3$  opacity in the blue and  $\text{O}_2$  and  $\text{H}_2\text{O}$  absorption bands in the red are accessible to *Gaia*; existing PSs have usually been designed for specific spectral type intervals or specific objects, while *Gaia* photometry must deal with the entire HR diagram, must allow taxonomy classification of Solar system objects and must be able to identify quasars and galaxies. In addition, *Gaia* allows the extension of stellar photometry to Galactic areas where the classical classification schemes may be no longer fully valid because of systematic variations in element abundances in stellar atmospheres and in interstellar matter. Finally, *Gaia* has to astrophysically characterize objects over a very large range of brightness, from  $G \sim 6$  to the faint limit of  $G_{\text{lim}} \sim 20$ , and consequently the width of the passbands will reflect a trade-off between sensitivity to physical parameters and the possibility to measure faint stars. Therefore, designing a new PS is the best approach to ensuring that the ambitious goals of *Gaia* will be achieved. This became clear early on when initial efforts to use existing PSs showed that these failed to cover all *Gaia* requirements. A fairly complete census of existing PSs can be found in Straižys (1992); Moro & Munari (2000); Fiorucci & Munari (2003); Bessell (2005).

Criteria for the design of a new PS have to be established a priori. As it is widely known, narrow passbands are very efficient in measuring specific spectral features, but have low performance for faint objects; broad passbands yield low photon-noise for faint objects but cannot give one-to-one determination of APs. The UV contains important information on APs, but *Gaia* will not be able to measure faint red objects in this spectral range. Therefore, a compromise between the different options (number, location, and width of the passbands and their total exposure time) is needed to achieve a PS that is maximally capable of separating objects with different APs in filter flux space. Such a PS should allow both accurate *discrete source classification* (i.e. identification of stars, galaxies, QSOs, Solar system objects, etc.) and *continuous parametrization* (values of APs, e.g. for stars  $T_{\text{eff}}$ ,  $[\text{M}/\text{H}]$ , etc.) for all *Gaia* targets across the AP space.

#### 4.1 Principles for the design

Over the years of mission study and development, the instrumental concept of *Gaia* has evolved. As a consequence, the requirements and constraints for designing the PS have evolved in terms of the number of passbands, the exposure time available per passband, the wavelength coverage in BBP and MBP, the spatial resolution of Astro and Spectro, the goals of BBP and MBP, and the complementarity of BBP, MBP and RVS measurements, etc.

With the consolidation of the study phase of the *Gaia* instrument design, the requirements for BBP and MBP are stabilized. The PS accepted as the baseline for the mission and presented in this paper is based on the following constraints.

- (i) The instrument design is as described in Section 2.
- (ii) Photometry from Astro has to account for chromaticity in order to achieve microarcsec astrometry, which implies a measurement of the SED of each object with contiguous broad passbands covering the whole wavelength range of the *G* passband (see Section 5.1.2).
- (iii) The photometry from Spectro has to provide the astrophysical characterization of the observed objects.
- (iv) The photometry from Astro has to provide the astrophysical characterization of the observed objects in dense fields (at stellar densities larger than 200 000–400 000 stars deg<sup>-2</sup>; mainly in the bulge, some Galactic disc areas and globular clusters).
- (v) One of the medium passbands in Spectro has to measure the flux in the wavelength range covered by RVS (848–874 nm).
- (vi) The trigonometric parallax is available and has to be used to constrain the luminosity (or the absolute magnitude).
- (vii) The information from RVS is not used for designing the PS because of the different limiting magnitude and spatial resolution of that instrument (in the actual *Gaia* data processing it is foreseen that astrometry, photometry and RVS measurements will be used together to derive APs, when possible).
- (viii) The *Gaia* PS is optimized for single stars, where priority is given to those types crucial for achieving the *Gaia* core science case, namely the unravelling of the structure and the formation history of the Milky Way. These stars are named ‘scientific photometric targets’ or simply ‘scientific targets’ (STs; see Section 4.3) and they constitute our test population.
- (ix) Every ST is characterized by its APs, where we consider  $T_{\text{eff}}$ ,  $\log g$ , chemical composition and  $A_V$ .<sup>2</sup> The chemical composition is described by the metallicity, [M/H], and the  $\alpha$ -element enhancements, [ $\alpha$ /Fe].
- (x) The error goals for the AP determination are established for every ST ( $\sigma_{k,\text{goal}}$ ; see Section 4.2 and Appendix A).
- (xi) The actual performance of a given PS with respect to the error goals is measured using an objective ‘FoM’ (see Section 4.2 and Appendix A).
- (xii) The global degeneracies of the PS have to be evaluated (see Section 4.5).
- (xiii) Additional merits such as, for example, the performance with respect to discrete object classification, the performance for non-ST objects, etc. have to be considered.

The procedure to come to a baseline PS (Brown et al. 2004) is based on the maximization of this ‘FoM’, a minimization of the global degeneracies and an evaluation of additional merits.

<sup>2</sup> Throughout the paper  $A_V$  means  $A_{\lambda=550}$ , i.e. the monochromatic interstellar extinction at  $\lambda = 550$  nm.

#### 4.2 Figure of merit

For a given PS, the FoM is constructed by calculating for each ST and each of its APs,  $p_k$ , the ratio  $\sigma_{k,\text{post}}/\sigma_{k,\text{goal}}$ . Here,  $\sigma_{k,\text{post}}$  is the estimate of the error that can be achieved with the given PS for  $p_k$  and  $\sigma_{k,\text{goal}}$  is the above mentioned error goal. The procedure for estimating  $\sigma_{k,\text{post}}$  and the definition of the FoM were proposed by Lindegren (2003b). For a given AP,  $p_k$  and a PS with measured fluxes  $\phi_j$  ( $j = 1, n$  passbands),  $\sigma_{k,\text{post}}$  is estimated using the sensitivity of the PS to that parameter ( $\partial\phi_j/\partial p_k$ ) and the errors of the photometric observations ( $\epsilon_j$ ). The latter are based on the noise model for the instrument–PS combination (see Section 6.2). The details are given in Appendix A.

The global FoM as given in equation (A6) in Appendix A is a weighted sum of the individual FoMs of every ST, which in turn are weighted sums of the ratios  $\sigma_{k,\text{post}}/\sigma_{k,\text{goal}}$  for each of the APs  $p_k$  (equation A4). A higher value of this FoM indicates a better performance for the given PS. The global FoM thus describes the performance of a PS across the HR diagram by taking into account the errors that can be achieved and the relative priorities of the different STs and their APs. The local degeneracies in the AP determinations (i.e. correlations between the errors for different APs for a given ST, see Section 4.5) are also taken into account in the FoM formalism. Each local degeneracy between APs leads to increased standard errors  $\sigma_{k,\text{post}}$  and thus a lower FoM.

In our implementation, the derivatives  $\partial\phi_j/\partial p_k$  and the error estimates  $\sigma_{k,\text{post}}$  are calculated numerically from simulated photometric data (Section 6.1). The calculation thereof requires (synthetic) SEDs of the STs and a noise model for the photometric instruments. The matrix  $\mathbf{B}$  from equation (A3) includes the a priori information for the AP vector  $\mathbf{p}$  and, in our case, corresponds simply to the range of possible values of the parameters  $p_k$ . The information from the parallax and its error is incorporated into  $\mathbf{B}$  following Lindegren (2004). Other information could be added (known reddening in a certain Galactic location, ranges of abundances according to Galactic population, etc.), but this would introduce our preconceptions of the structure and stellar populations of the Galaxy into the PS design and we therefore did not include such constraints.

The MBP data will have a lower spatial resolution than the BBP data. For non-crowded regions on the sky (with respect to MBP), we assume that the MBP and BBP photometry will always be combined for the estimation of APs. Hence, the calculation of the achievable posterior errors is always done by combining BBP and MBP data. For dense stellar fields, only BBP data will be available and, in that case, the achievable AP errors and the FoM have been computed using only broad-band photometry.

SEDs of the STs in the test population were taken from the BASEL 2.2 (Lejeune, Cuisinier & Buser 1998), NEXTGEN (Hauschildt, Allard & Baron 1999) and MARCS<sup>3</sup> (Gustafsson et al. 2003) libraries. The BASEL 2.2 library is a compilation of synthetic spectra from libraries published by Kurucz (1979), Bessell et al. (1989), Fluks et al. (1994) and Hauschildt et al. (1999). It covers the whole HR diagram and [M/H] abundances from  $-5$  to  $+1$  dex, but with solar  $\alpha$ -element abundances. A new version of the NEXTGEN library (NEXTGEN 2) has been built taking into account *Gaia* mission needs (Hauschildt et al. 2003). This library includes SEDs for stars cooler than 10 000 K with [M/H] ranging from  $-2$  to  $+0$  dex and [ $\alpha$ /Fe] from  $-0.2$  to  $+0.8$  dex. A more extended grid is currently available (Brott & Hauschildt 2005). Finally, a new version of the MARCS

<sup>3</sup> See also <http://marcs.astro.uu.se>

library taking into account non-solar  $\alpha$ -element abundances has been created specifically for *Gaia* studies. This library provides coverage between 3000 and 5000 K,  $[M/H]$  from  $-4$  to  $+0.5$  dex and  $[\alpha/Fe]$  from  $+0$  to  $+0.4$  dex.

Empirical libraries, like those by Gunn & Stryker (1983) and Pickles (1998), do not provide full coverage of the HR diagram and the corresponding chemical composition range and, therefore, they are not appropriate for computing the FoM values.

Finally, we would like to make a few remarks here about the interpretation of the calculated values of  $\sigma_{k,\text{post}}$  and the corresponding FoM for a set of proposed PSs. The values of  $\sigma_{k,\text{post}}$  calculated as described in Appendix A should not be taken as the actual errors that will be achieved by the *Gaia* PS. They represent the achievable precision if the synthetic spectra represent the true stars and if the noise model is correct. This issue is discussed more thoroughly in Section 7. What makes the FoM a powerful tool is that it enables an objective *comparison* of different PS proposals, based on a set of agreed error goals and scientific priorities. In addition, for each PS, a detailed study can be made of its strengths and weaknesses as compared with other PSs by examining the FoM for individual STs and for groups of STs (such as specific types of stars, populations in certain Galactic directions, bright versus faint stars, reddened versus unreddened, etc.). Once the best PS proposal has been chosen it can be further tuned by using the FoM procedure to improve its sensitivity to certain APs or to improve the performance for certain groups of stars. This objective FoM approach has not been used before in the design of a PS.

### 4.3 Test population and error goals

According to the scientific goals of *Gaia* (see Table 2), for every Galactic stellar population, several kinds of stars were selected as STs and a priority, expressed as a numerical weight, was assigned to them (Jordi et al. 2004d,e). These stars have been considered in different directions in the Milky Way (toward the centre, the anticentre and perpendicular to the Galactic plane) and at different distances (0.5, 1, 2, 5, 10 and 30 kpc) in accordance with a Galaxy model (Torra et al. 1999). The STs have been reddened according to a 3D interstellar extinction model (Drimmel, Cabrera-Lavers & López-Corredoira 2003), assuming a standard extinction law ( $R_V =$

3.1). Bulge stars in areas of high and low interstellar extinction were also included. This results in a set of about 6500 targets each with a parallax error estimated from its colour and apparent magnitude (ESA 2000). The targets in the halo are considered to have  $[M/H]$  abundances from  $-4$  to  $-1$  dex and  $[\alpha/Fe]$  abundances from  $+0.2$  to  $+0.4$  dex; for the thick-disc targets,  $[M/H]$  ranges from  $-2$  to  $0$  dex and  $[\alpha/Fe]$  from  $0.0$  to  $+0.2$  dex; for the thin-disc targets  $[M/H]$  ranges from  $-1$  to  $+0.5$  dex and  $[\alpha/Fe]$  from  $-0.2$  to  $0.0$  dex; and, finally, for the bulge targets, we assume the same range for  $[M/H]$  as for the thin disc and  $[\alpha/Fe]$  ranges from  $0$  to  $0.4$  dex. The ranges of temperatures and absolute luminosities are assigned according to the specific range of ages of each stellar population. The values of  $T_{\text{eff}}$  range from 3000 to 40 000 K and the values of  $\log g$  are in the range  $0.0$ – $5.0$  dex.

We adopted the following precision goals ( $\sigma_{k,\text{goal}}$ ).

- (i)  $T_{\text{eff}}$  for A–M stars:  $\sigma_{T_{\text{eff}}}/T_{\text{eff}} = 1$ – $2$  per cent.
- (ii)  $T_{\text{eff}}$  for O–B stars:  $\sigma_{T_{\text{eff}}}/T_{\text{eff}} = 2$ – $5$  per cent.
- (iii)  $A_V$ :  $\sigma_{A_V} = 0.1$  mag at  $A_V \leq 3.0$  mag,  $\sigma_{A_V} = 0.5$  mag at  $A_V > 3.0$  mag.
- (iv)  $M_V$  for stars with  $\sigma_{\pi}/\pi \leq 10$  per cent: assumed known.
- (v)  $\log g$  for stars with  $\sigma_{\pi}/\pi > 10$  per cent:  $\sigma_{\log g} = 0.2$  dex.
- (vi)  $[M/H]$  (not to be determined for OB stars and supergiants):  $\sigma_{[M/H]} = 0.1$  dex.
- (vii)  $[\alpha/Fe]$ :  $\sigma_{[\alpha/Fe]} < 0.3$  dex.
- (viii) Asymptotic giant branch (AGB): carbon/oxygen classification.

### 4.4 Photometric system proposals

In this paper, we discuss in detail only the baseline PS for *Gaia* that results from the optimization process described above. However, many proposals for a PS for *Gaia* have been studied.

Different approaches have been used for the definition of the passbands. Grenon et al. (1999), Munari (1999), Straižys, Høg & Vansevičius (2000), Vansevičius & Bridžius (2002, 2003), Lindegren (2003a) and Jordi et al. (2003, 2004c) based their BBP and/or MBP proposals on their astrophysical expertise and/or the performance of the existing PSs. Tautvaišienė, Edvardsson & Bartašiūtė (2003) and Tautvaišienė & Edvardsson (2005) provided

**Table 2.** The main science goals for *Gaia* concerning Galactic structure and evolution studies and the main corresponding tracers, from the ‘*Gaia* Concept and Technology Study Report’ (ESA 2000).

Science goal	Main tracers
Chemical abundance galactocentric distribution	G and K giants
Galactocentric age gradients, star formation rate	HB stars, early-AGB, main-sequence turn-off stars
Disentangling age–metallicity degeneracy	Main-sequence turn-off, subgiants
Star formation history	Main-sequence stars earlier than G5 V, subgiants
Detailed knowledge of luminosity function	Low main-sequence stars
Halo streams, age and chemical abundance determinations	G and K giants
Outer halo ( $R > 20$ kpc), accretion and merging	G and K giants and HB stars
Earliest phases of evolution of the Galaxy	Most metal-poor stars, C- subgiants and dwarfs near the turn-off
Distance scale	RR Lyrae, Cepheids
Thick-disc formation mechanism (pre- versus post-thin disc)	G and K giants, HB stars
Merging and/or diffusion	High velocity A-type stars
‘In situ’ gravitational potential, $K_z$ , age–velocity relation	F–G–K dwarfs
Large-scale structure (warp, asymmetry)	K–M giants
Interstellar medium distribution	O–F dwarfs
Large-scale structure (spiral arms, star-formation regions)	OB stars, supergiants
Star formation rate in the bulge	Red giant branch, asymptotic giant branch
Shape of the bulge, orientation, bar	Red giant branch, asymptotic giant branch, red clump stars

guidelines for designing a PS sensitive to C, N, O and  $\alpha$ -process elements. We note that the sets of filters by Grenon et al. (1999), Munari (1999), and Straižys et al. (2000) were designed with substantially different constraints imposed in early phases of the *Gaia* instrument design.

Bailer-Jones (2004) developed a novel method for designing PSs via a direct numerical optimization. By considering a filter system as a set of free parameters (central wavelengths, FWHM etc.), it may be designed by optimizing an FoM with respect to these parameters. This FoM is a measure of how well the filter system separates the stars in the data space and of how much it avoids degeneracies in the AP determinations. The resulting filter systems tend to have rather broad and overlapping passbands and large gaps in between at the same time. Some commonalities with conventional PSs may be recognized. Although first analyses showed these systems to yield FoM values only slightly inferior to conventional PS proposals, the method was considered too novel and further studies were not pursued.

Lindegren (2001) proposed several BBP systems, differing in the number of passbands and their profiles, and tested their performance with respect to chromatic effects estimation. He concluded that five passbands do not provide a clear advantage over four passbands and that the overlapping of the passbands is more important.

Heiter et al. (2005) used the Principal Components Analysis technique to design a set of BBP passbands that is optimal for a subset of STs with effective temperatures between 3000 and 5000 K. Photometry was simulated for a grid of sets of four broad filters each. The FWHMs were varied in equidistant steps, while the central wavelengths were determined by requiring contiguous filters covering the whole wavelength range. The resulting set of passbands was found to perform better than all other proposals for bulge stars but worse than all others when evaluated for the complete set of STs (Jordi et al. 2004a).

All proposed PSs were evaluated using the FoM procedure and the results were returned to the proposers who were then given the opportunity to refine their respective PSs and submit improved versions as a new PS proposal. Updates of the PSs above or new ones came out of every evaluation cycle (Høg & Knude 2004a,b; Jordi & Carrasco 2004a,b; Knude & Høg 2004; Straižys, Zdanavičius & Lazauskaite 2004). Finally, after several trials for the fine tuning of a few individual passbands, the C1B and C1M sets (Jordi et al. 2004a,b) were adopted as the baseline PS for *Gaia*. Detailed results of the evaluation of all PS proposals can be found in Jordi et al. (2004a,b).

#### 4.5 Local and global degeneracies

The goal of designing a PS that allows both accurate discrete classification and continuous parametrization of observed sources translates to demanding that the degeneracies in the PS are minimized.

The discrete classification problem concerns the way very different parts of AP space are mapped by the PS into the filter flux space. For example, due to extinction, a highly reddened O star may to first order look like a nearby unreddened cool dwarf. A good PS should as much as possible be free of such ‘global’ degeneracies. The continuous parametrization problem concerns the way a PS maps a small region around a certain object in AP space onto filter fluxes. Here, it is the ‘local’ degeneracies that are important. Examples include the well-known degeneracy between  $T_{\text{eff}}$  and  $A_V$  and the difficulty of disentangling the effects of  $T_{\text{eff}}$  and  $\log g$  for a PS without passbands shortwards of the Balmer jump.

Our method of evaluating the proposed PSs as outlined in Section 4.2 focuses on the local degeneracies. Consider the gradient vectors that describe how the filter fluxes respond to changes in particular APs. For a good PS, these gradients should be large with respect to the noise in the data and they should ideally be orthogonal to each other, where the orthogonality is also defined with respect to the noise (i.e. for the gradients with components  $1/\epsilon_j \times \partial\phi_j/\partial p_k$ , see Appendix A). Large gradients mean that the PS is sensitive to the corresponding APs while their orthogonality ensures that there are no local degeneracies. The FoM takes this into account by calculating the posterior errors on estimated APs using the sensitivity matrix which contains these gradient vectors (see Appendix A for more details). Small gradient vectors are reflected in larger errors on the estimated AP. Non-orthogonal gradient vectors will also lead to larger errors and to non-zero covariances (i.e. correlated errors) in the posterior variance–covariance matrix of the estimated APs. Both effects will lead to a lower FoM (this is explained in more detail in Appendix A).

The FoM calculations do not take global degeneracies into account. In fact, it is assumed that one already has available a good classification of the object to be parametrized so that the linearized equations from which the FoM is derived apply. The global degeneracies reflect the highly non-linear mapping from AP space to filter flux space and are difficult to characterize in practice.

We attempted to compare the different PS proposals with respect to global degeneracies by employing self-organizing maps to explore how the different STs cluster in data space and how well they can be separated. The results were inconclusive as the different PS proposals showed rather similar behaviour. This is plausible because to first order all the proposed filter systems were similar. The sets of BBP passbands were very much alike and the sets of MBP passbands all had a set of blue and a set of red filters with a gap between these sets from  $\sim 550$  to  $\sim 700$  nm and they all had an  $H\alpha$  filter in this gap. With a continuous sampling of stellar parameters, a filter system will define a complex manifold in the space of filter flux vectors onto which each star will be mapped. It is the overall shape of this manifold that determines the presence or absence of global degeneracies in the PS. Hence, it may be that the filter systems that had been considered all define roughly the same manifold, the differences between filter systems only being manifest at the local level (where the FoM calculations are more relevant).

Characterizing the global degeneracies will be an important task in the context of the automatic classification effort for the *Gaia* data processing. A full understanding of the behaviour of the *Gaia* PS is essential for setting up appropriate discrete classification and continuous parametrization algorithms.

## 5 THE *Gaia* PHOTOMETRIC SYSTEM

In this section, we describe in detail the baseline PS for *Gaia*, called C1, which consists of the C1B and C1M broad and medium passbands. The role of each of the passbands is described in relation to spectral features and astrophysical diagnostics.

### 5.1 The C1B broad passbands

The C1B component of the *Gaia* PS has five broad passbands covering the wavelength range of the unfiltered light from the blue to the far-red (i.e. 400–1000 nm). The basic response curve of the filters versus wavelength is a symmetric quasi-trapezoidal shape. The filters were chosen to satisfy both the astrophysical needs and the specific requirements for chromaticity calibration of the astrometric



**Table 3.** Specifications of the filters of C1B implemented in Astro.

Band	C1B431	C1B556	C1B655	C1B768	C1B916
$\lambda_{\text{blue}}$ (nm)	380	492	620	690	866
$\lambda_{\text{red}}$ (nm)	482	620	690	846	966
$\lambda_c$ (nm)	431	556	655	768	916
$\Delta\lambda$ (nm)	102	128	70	156	100
$\delta\lambda$ (nm)	10,40	10,10	10,10	10,40	40,10
$\epsilon$ (nm)	2,2	2,2	2,2	2,2	2,2
$T_{\text{max}}$ (per cent)	90	90	90	90	90
$n_{\text{strips}}$	1	0.5	1	0.5	1

$\lambda_{\text{blue}}$ ,  $\lambda_{\text{red}}$ : wavelengths at half-maximum transmission.  $\lambda_c$ : central wavelength =  $0.5(\lambda_{\text{blue}} + \lambda_{\text{red}})$ .  $\Delta\lambda$ : FWHM.  $\delta\lambda$ : edge width (blue, red) between 10 and 90 per cent of  $T_{\text{max}}$ .  $\epsilon$ : manufacturing tolerance intervals centred on  $\lambda_{\text{blue}}$  and  $\lambda_{\text{red}}$ .  $T_{\text{max}}$ : maximum transmission of filter.  $n_{\text{strips}}$ : number of CCD strips carrying the filter: C1B556 and C1B768 share one CCD strip.

instrument (see Section 4). The C1B set of passbands evolved from the convergence of the Lindegren (2003a), Jordi & Carrasco (2004a) and Straizys (2004) proposals. The specifications of the filters are given in Table 3. Fig. 5 shows the spectral response of the passbands. The estimated end-of-mission precisions, computed as described in Section 6.2, are shown in Fig. 6.

The Balmer discontinuity and the H $\beta$  line limit the blue and red edges of the C1B431 filter, respectively. The reddest filter C1B916 is designed to measure the light between the Paschen jump and the red limit of the sensitivity of CCDs in the Astro focal plane. The filter C1B655 is centred on the H $\alpha$  line and its width has been optimized together with C1M656 in C1M (see Section 5.2). The blue and red limits of the two remaining filters (C1B556 and C1B768) are consequently set in order to provide full coverage of the wavelength range in *G* (i.e. avoiding gaps between passbands). Four passbands are

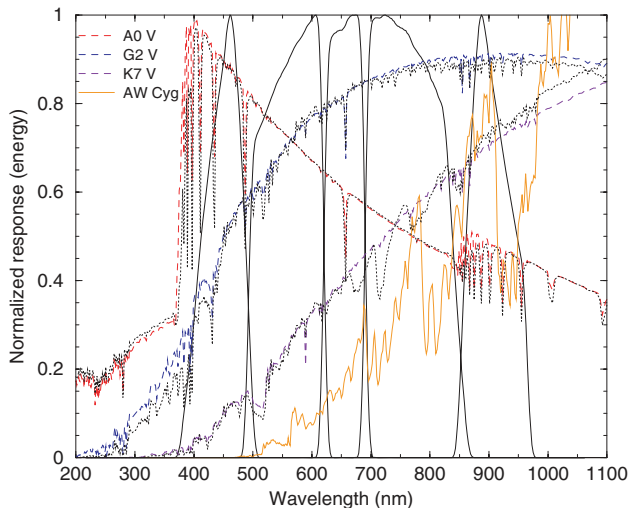


**Figure 5.** Response curves of the filters in C1B folded with the optics transmission and the QE of the CCDs. The spectral energy distributions of solar metallicity A0 V–, G2 V– and K7 V–type stars in units of  $\text{W m}^{-2} \text{Hz}^{-1}$ , taken from the BaSeL 2.2 library, are overplotted with (black) dotted lines (the vertical scale is arbitrary). The dashed (blue and violet) lines correspond to G2 V– and K7 V–type stars with  $[M/H] = -1$  (when compared with the dotted lines they show the effect of a change of  $[M/H]$ ). The dashed (red) line shows the change of the spectrum of an A0-type star due to a change of luminosity. The solid (orange) line is the N-type carbon star AW Cyg extracted from the Gunn & Stryker (1983) library of stellar spectra.

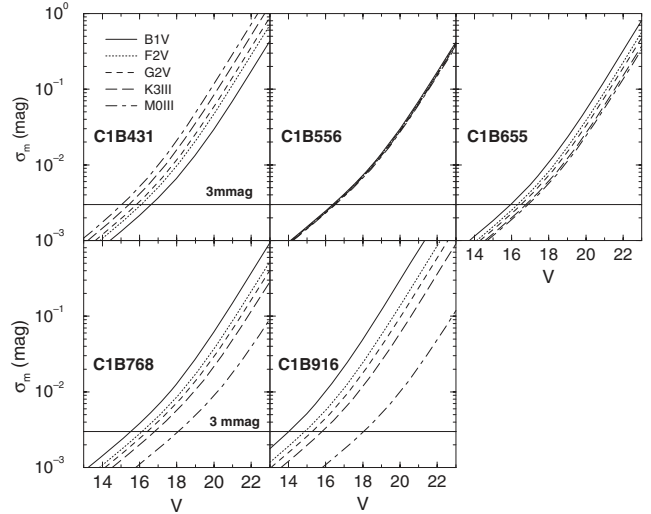


**Figure 6.** Estimation of the end-of-mission precisions for the five passbands in C1B as a function of  $V$ , computed according to equation (2) and taking  $\sigma_{\text{cal}} = 0$  mag. In this paper, the contribution of calibration errors to the end-of-mission precision is estimated to be 3 mmag in every passband (horizontal line). The errors for C1B556 are all nearly the same for a given  $V$  magnitude because the mean wavelengths of these passbands are very similar.

enough for chromaticity calibration, but five passbands are preferred to four, when the classification and astrophysical parametrization of stars is considered. Because only four strips of CCDs are available in BBP, the two broadest passbands (C1B556 and C1B768) are implemented together in one strip. Hence, the number of observations with these two passbands will be half as much as with the other C1B passbands.

The current design of the payload foresees no UV sensitivity for the Astro/BBP instrument (see Section 2). The near UV is the most important for stellar classification. The Balmer jump is the feature in the spectra of B–A–F–type stars most sensitive to the temperature and gravity. It also contains information on the metallicity of F–G–K–type stars. The absence of an UV passband in BBP is compensated with the inclusion of a broad UV passband (C1M326) in MBP (see Section 5.2). The classification and parametrization of objects in *Gaia* is done using the BBP and MBP measurements together and therefore the lack of a UV passband in BBP should not be a drawback. However, because the Spectro instrument has a lower angular resolution than Astro, the combination of BBP and MBP data is not always possible. BBP will be the only tool for classification of stars in the crowded fields with stellar densities larger than  $200\,000\text{--}400\,000$  stars  $\text{deg}^{-2}$  (see Section 6.3). Such stellar densities are found in some areas of the bulge and of the disc (Drimmel et al. 2005; Robin et al. 2005) and most of these areas have low interstellar extinction (such as Baade’s window). In dense areas, the trigonometric parallax and the Paschen jump will provide luminosity parametrization.

### 5.1.1 Astrophysical diagnostics

The response of the C1B431 filter at the shortest wavelength is asymmetrical, with a red edge that is less steep. This is done to compensate the shift of the maximum of the response function redwards due to the slope of the QE curve and the reflectance curve for six silver surfaces. As a result, the response function of the C1B431 passband becomes similar to that of the *B* passband of the *UBV*

system. The mean wavelengths of both passbands are also similar: 445 nm for C1B431 and 442 nm for *B*.

The mean wavelength and half width of the C1B556 response function are very similar to that of the *V* passband. As a result, the colour index C1B431–C1B556 will be easily transformable to Johnson’s *B–V* and vice versa. Analogously, the C1B768 passband can be easily related with the Cousins *I*, the Sloan Digital Sky Survey (SDSS) *i'* and the *Hubble Space Telescope (HST)* 814 passbands, and the colour index C1B556–C1B768 is transformable to  $V - I_C$ ,  $r' - i'$  and *HST* 555–814. This will facilitate the comparison of the numerous ground-based investigations in the *BV* system and the large number of observations being done in the far-red passbands with the *Gaia* results. As can be seen from Fig. 5, the differences of the ‘blue minus green’, ‘blue minus red’ or ‘blue minus far-red’ magnitudes may serve as a measure of metallic-line blanketing, although with much less sensitivity than a colour index containing the UV. In the C1B431–C1B556 versus C1B556–C1B768 diagram, the deviations of F–G metal-deficient dwarfs and G–K metal-deficient giants from the corresponding sequences of solar metallicity are up to 0.07 and 0.20 mag, respectively.

The combination of the fluxes measured in the C1B655 passband and the narrow passband C1M656 in MBP form an  $H\alpha$  index primarily measuring the strength of the  $H\alpha$  line. The  $H\alpha$  index shares the same properties as the  $\beta$  index in the Strömgren–Crawford PS. It is an indicator of luminosity for stars earlier than A0 and of temperature for stars later than A3, almost independent of interstellar extinction and chemical composition. The same reddening-free index may be used for the identification of emission-line stars.

The two remaining red and far-red passbands, C1B768 and C1B916, give the height of the Paschen jump which is a function of temperature and gravity. Although the maximum height of the Paschen jump is 0.3 mag only, i.e. about 4 times smaller than the Balmer jump, it still provides the needed information if its height, C1B768–C1B916, is measured with high accuracy (not lower than 1 per cent) and this is reachable up to about  $V \sim 17$ –18 (see Fig. 6). The colour indices C1B556–C1B768 and C1B556–C1B916 for unreddened late-type stars may be used as indicators for the temperature. These colour indices (and C1B768–C1B916) also allow for the separation of cool oxygen-rich (M) and carbon-rich (N) stars.

The C1M326–C1B431 versus C1B431–C1B556 diagram has the same properties as the  $U - B$  versus  $B - V$  diagram of Johnson’s system or similar diagrams for other systems (Straižys 1992). Supergiants are well separated from the main-sequence stars. Metal deficient F–G dwarfs and G–K giants exhibit UV excesses up to 0.4 mag. Blue horizontal branch stars show UV deficiencies up to 0.3 mag, while white dwarfs are situated around the interstellar reddening line of O-type stars.

### 5.1.2 Chromaticity evaluation

Although no refracting optics are used for the astrometric field, the precise centre of a stellar image is still wavelength dependent because of diffraction and its interplay with the optical aberrations of the instrument. Differential shifts by up to  $\sim 10$  per cent of the width of the diffraction image (i.e. several milliarcsec) may be caused by odd aberrations such as coma, even though the resolution remains essentially diffraction limited. As a result, the measured centres of stellar images will depend on their SEDs, and a careful calibration of the effect, known as *chromaticity*, is mandatory in order to attain the astrometric accuracy goals. The gross SED of each observed target is

therefore needed in the wavelength range of the astrometric CCDs; moreover, these data are needed with the same spatial resolution as in the astrometric field. As stated before, the BBP set of passbands was designed with this requirement in mind, as well as on astrophysical grounds.

Lindgren (2003c) showed that, for the chromaticity calibration, near-rectangular filters are acceptable and that the choice of the separation wavelengths is more important than the edge widths. The author concluded that the use of four broad passbands covering the wavelength range of the astrometric *G* passband should be enough to match the chromaticity constraints (rms contribution to the parallaxes  $< 1 \mu\text{as}$ ).

Following the design of the passbands in C1B, a more detailed evaluation of residual chromaticity effects was performed. A worst-case scenario, representing an extreme amount of coma, was considered where the wavefront aberration consisted of a third-degree Legendre polynomial in the normalized along-scan pupil coordinate, with rms wavefront error (WFE) 45 nm. Polychromatic images in *G* were generated for a library of synthetic stellar spectra (Munari et al. 2005), including some reddened by interstellar extinction. Image centres were computed through a modified form of Tukey’s biweight formula (Press et al. 1992), with properties similar to the maximum-likelihood estimator to be used with the real *Gaia* data.

Fig. 7 shows the stellar image shifts for a range of synthetic stellar spectra plotted versus one of the BBP colour indices. For the particular WFE assumed in this example, there is a general shift of the image centroid by  $\sim 4 \text{ mas}$  caused by the coma. However, it is only the variation of this shift with the spectral composition that is of concern here. The rms variation of the shift versus colour index is  $415 \mu\text{as}$ . Using linear regression against the synthetic stellar C1B counts  $\phi_j$  ( $j = 1 \dots 5$ , normalized to  $\sum_j \phi_j = 1$ ), the shifts could be reproduced with an rms residual of  $7 \mu\text{as}$ . Further averaging between the  $\sim 800$  astrometric CCD observations that are combined in a single parallax will reduce the astrometric effect of the chromatic residuals by a factor 0.02–0.2 depending on the degree of correlation among the individual observations, thus leading to a chromatic contribution to the parallax errors of 0.14–1.4  $\mu\text{as}$ . Because these numbers are based on a worst-case assumption for the WFE and a somewhat simplistic calibration model, it is reasonable to expect that a residual contribution of  $1 \mu\text{as}$  can be achieved and, in particular, that the chosen C1B passbands provide sufficient information

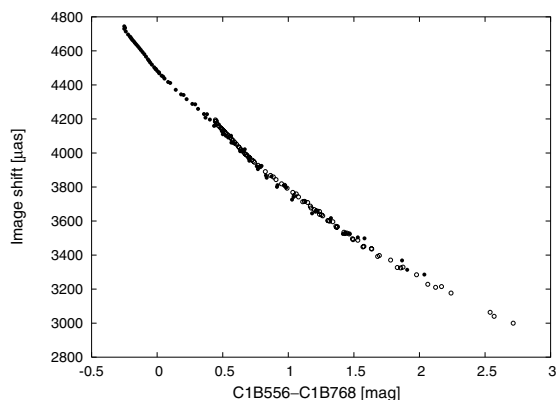


**Figure 7.** An example of the colour-dependent shifts (chromaticity) of stellar images that may be obtained in the astrometric field as the result of a coma-like optical aberration (see text for details). The shift relative to the geometric image centre is plotted versus a  $(V - I_C)$ -like colour index for a range of synthetic stellar spectra without extinction (filled circles) and for  $A_V = 2 \text{ mag}$  (open circles).

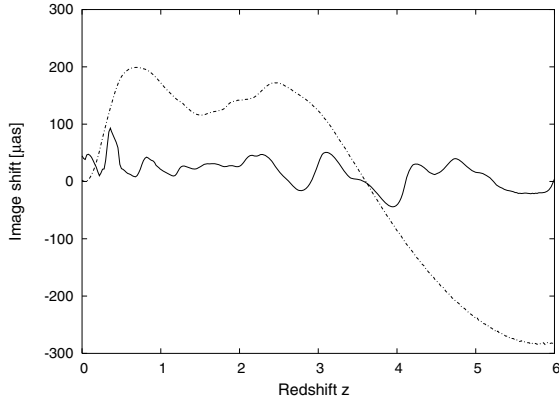


**Figure 8.** The chromatic shifts of a quasar image before (dash-dotted curve) and after (solid) correction for the effect calibrated by means of stellar spectra. A standard quasar spectrum was assumed to be observed at different redshifts and subject to the same aberrations as in Fig. 7. (The dash-dotted curve has been displaced 4000  $\mu\text{as}$  downwards in the diagram to offset the overall shift caused by the coma.)

on the SED within the *G* passband for this purpose. The residual effect is thus small compared with the statistical errors from photon noise and other sources even for bright stars.

The chromaticity correction based on an empirical calibration against stellar BBP fluxes will be less accurate for objects with strongly deviating SEDs. Prime examples of this are the quasars, which may exhibit strong emission lines at almost any wavelength depending on redshift. Quasars are astrometrically important for establishing a non-rotating extragalactic reference system for proper motions; thus, chromaticity correction must work also for these objects. This was investigated by applying the correction derived as described above from stellar spectra to synthetic quasar images, calculated from a mean quasar spectrum observed at redshifts in the range  $z = 0$  to 6. Fig. 8 shows the uncorrected image shift as function of  $z$  (dash-dotted curve) together with the residual shift

after correction (solid curve). The rms image shift decreases from 170  $\mu\text{as}$  before to 29  $\mu\text{as}$  after correction. The residual curve shows artefacts that are clearly attributable to the limited sampling of the spectral range. For example, the negative slopes for  $z = 2.3$ – $2.8$  and  $z = 3.1$ – $3.9$  correspond to the redshifted Lyman- $\alpha$  emission line moving through the C1B431 and C1B556 passbands, respectively.

With similar assumptions as for the stars concerning the statistical averaging of the effect when propagating to the astrometric parameters, the residual effect for the quasars will be a few microarcsec. This is acceptable because these are mostly faint objects with much larger photon-statistical errors.

Note that the data in Figs 7–8 only represent an example of the image shifts that may occur. The actual behaviour depends strongly on the shape and size of WFE, which vary considerably across the field of view, and on the detailed centroiding algorithm.

## 5.2 The C1M medium passbands

The C1M component of the *Gaia* PS consists of 14 passbands and evolved from the convergence of the proposals by Grenon et al. (1999), Vasevičius & Bridžius (2002), Knude & Høg (2004), Jordi & Carrasco (2004b) and Straižys et al. (2004). The guidelines by Tautvaišienė & Edvardsson (2002) for  $\alpha$ -element abundance determination were taken into account. The basic response curve of the filters versus wavelength is a symmetric quasi-trapezoidal shape. Their parameters are listed in Table 4 and the response of the corresponding passbands is shown in Fig. 9. Six strips with red-enhanced CCDs are available for MBP and six red passbands have been designed, implemented as one filter for each strip, with the only constraint that MBP has to measure the flux entering the RVS instrument (see Section 4.1). For the blue passbands, eight filters are implemented on the 10 strips with blue-enhanced CCDs. Two strips have been allocated to each of the two UV passbands to increase the S/N of the measurements.

The primary purpose of the medium passbands is the classification and astrophysical parametrization of the observed objects

**Table 4.** Specifications of the filters in C1M implemented in Spectro.

Band	C1M326	C1M379	C1M395	C1M410	C1M467	C1M506	C1M515
$\lambda_{\text{blue}}$ (nm)	285	367	390	400	458	488	506
$\lambda_{\text{red}}$ (nm)	367	391	400	420	478	524	524
$\lambda_{\text{c}}$ (nm)	326	379	395	410	468	506	515
$\Delta\lambda$ (nm)	82	24	10	20	20	36	18
$\delta\lambda$ (nm)	5	5	5	5	5	5	5
$\epsilon$ (nm)	2,2	2,2	2,1	1,2	2,2	2,2	2,2
$T_{\text{max}}$ (per cent)	90	90	90	90	90	90	90
Type of CCD	Blue	Blue	Blue	Blue	Blue	Blue	Blue
$n_{\text{strips}}$	2	2	1	1	1	1	1
Band	C1M549	C1M656	C1M716	C1M747	C1M825	C1M861	C1M965
$\lambda_{\text{blue}}$ (nm)	538	652.8	703	731	808	845	930
$\lambda_{\text{red}}$ (nm)	560	659.8	729	763	842	877	1000
$\lambda_{\text{c}}$ (nm)	549	656.3	717	747	825	861	965
$\Delta\lambda$ (nm)	22	7	26	32	34	32	70
$\delta\lambda$ (nm)	5	2	5	5	5	5	5
$\epsilon$ (nm)	2,2	1,1	2,2	2,2	2,2	2,2	2,2
$T_{\text{max}}$ (per cent)	90	90	90	90	90	90	90
Type of CCD	Blue	Red	Red	Red	Red	Red	Red
$n_{\text{strips}}$	1	1	1	1	1	1	1

$\lambda_{\text{blue}}$ ,  $\lambda_{\text{red}}$ : wavelengths at half-maximum transmission.  $\lambda_{\text{c}}$ : central wavelength =  $0.5(\lambda_{\text{blue}} + \lambda_{\text{red}})$ .  $\Delta\lambda$ : FWHM.  $\delta\lambda$ : edge width (blue, red) between 10 and 90 per cent of  $T_{\text{max}}$ .  $\epsilon$ : manufacturing tolerance intervals centred on  $\lambda_{\text{blue}}$  and  $\lambda_{\text{red}}$ .  $T_{\text{max}}$ : maximum transmission of filter.  $n_{\text{strips}}$ : number of CCD strips carrying the filter.

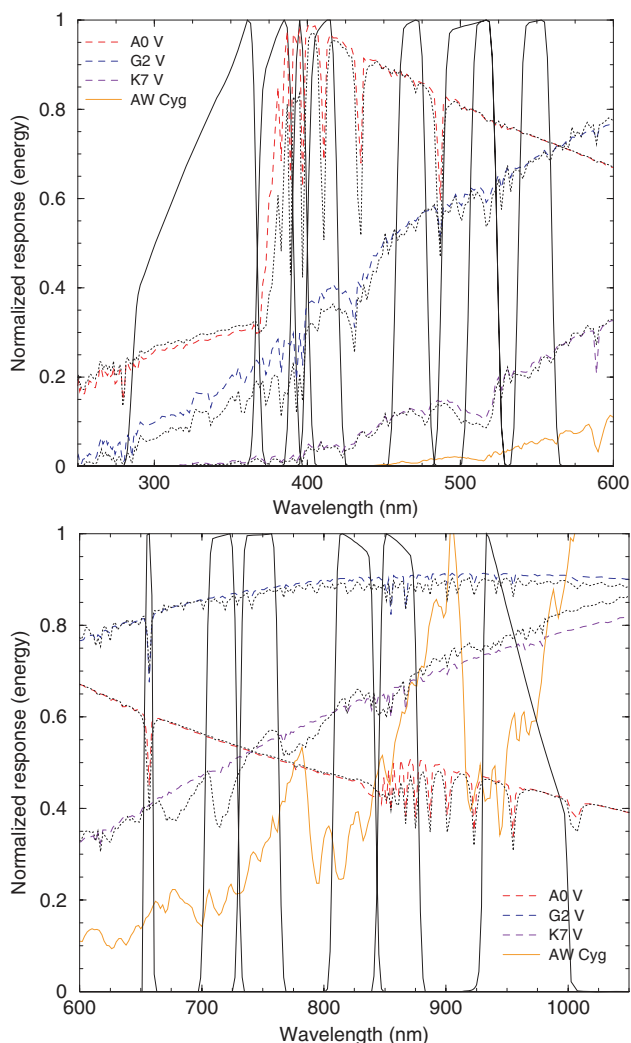


**Figure 9.** Same as Fig. 5 for C1M. Top and bottom figures show the ‘blue’ and ‘red’ passbands, respectively.

(stars, QSOs, galaxies, Solar system bodies, etc.). In the case of the stars, the goal is to determine effective temperature  $T_{\text{eff}}$ , gravity  $\log g$  or luminosity  $M_V$ , chemical composition  $[M/H]$ ,  $[\alpha/Fe]$  and C/O abundances, peculiarity type, the presence of emission, etc., in the presence of varying and unknown interstellar extinction. Taxonomy classification for Solar system objects and photometric redshift determination for QSOs are also aimed for.

### 5.2.1 Astrophysical diagnostics

The filter at the shortest wavelength is C1M326 with wavelengths at half-maximum transmission of 285 and 367 nm (thus it is of broad passband type although implemented in Spectro). Below 280 nm, strong absorption lines, metallicity dependent, are present already in A-type stars. The interstellar extinction increases rapidly below 280 nm and reaches a maximum at 218 nm. In space, the UV passband can be extended down to 280 nm, which improves the determination of  $[M/H]$  for F–G–K stars because of the presence of many atomic lines, ionized or of high excitation. For late G dwarfs, the line blocking in the extended UV passband is about 2.7 times larger than in the violet 376–430 nm domain. The red side of C1M326 is set at the Balmer jump. The colour indices C1M326–

C1B431 or C1M326–C1M410 give the height of the Balmer jump, which is a function of  $T_{\text{eff}}$  and  $\log g$  in B–A–F stars. In F–G–K stars, these colour indices measure metallic line blocking in the UV, which can be calibrated in terms of  $[M/H]$ .

The C1M379 passband is placed on the wavelength range where the lines corresponding to the higher energy levels of the Balmer series crowd together in early-type stars. The integrated absorption in these lines is very sensitive to  $\log g$  (or  $M_V$ ). For late-type stars, the position of this passband coincides with the maximum blocking of the spectrum by metallic lines. Hence, the colour index C1M379–C1M467 is a sensitive indicator of metallicity. Analogues in other PSs are the  $P$  magnitude in the Vilnius system and  $L$  in the Walraven system.

The C1M395 passband is introduced mainly to measure the Ca II H line. The index C1M395–C1M410 shows a strong correlation with  $W(\text{CaT}^*)$ , the equivalent width of the Calcium triplet measured by the RVS instrument, corrected for the influence of the Paschen lines. The C1M395–C1M410 versus  $W(\text{CaT}^*)$  may be used as a  $\log g$  estimator (Kaltcheva, Knude & Georgiev 2003, Knude & Carrasco, private communication). The C1M395–C1M410 versus  $W(\text{CaT}^*)$  plane is particularly useful because the effect of reddening on the colour index is only minor due to the small separation of the two passbands. Additional uses of the C1M395 passband are in assisting the  $[\alpha/Fe]$  determination and in the identification of very metal-poor stars.

The violet C1M410 passband measures the spectrum intensity redwards of the Balmer jump. In combination with C1M326, it gives the height of the jump. For K–M stars it is the shortest passband that, when combined with longer passbands, can provide temperatures and luminosities of solar metallicity stars in the presence of interstellar reddening (i.e. when the stars are too faint in the UV). Its analogues are:  $v$  in the Strömrgren system,  $B_1$  in the Geneva system and  $X$  in the Vilnius system.

The blue C1M467 and green C1M549 passbands measure domains where the absorption by atomic and molecular lines is minimal. The flux in these domains corresponds to a pseudo-continuum. The colour indices C1M467–C1M549, C1M467–C1M747 and C1M549–C1M747 may be used as indicators of the temperature for stars of all spectral types. The analogues of C1M467 are:  $b$  in the Strömrgren system,  $B_2$  in the Geneva system and  $Y$  in the Vilnius system. The analogues of C1M549 are:  $y$  in the Strömrgren system and  $V$  in the Vilnius system.

The green C1M515 passband is placed on a broad spectral depression seen in the spectra of G- and K-type stars and formed by crowding of numerous metallic lines. Among them, the strongest features are the Mg I triplet and the MgH band. The depth of this depression, the intensity of which reaches a maximum around K7 V, is very sensitive to gravity, being deeper in dwarfs than in giants. The same passband is also useful for the identification of Ap stars of the Sr–Cr–Eu type. The same passband ( $Z$ ) is used in the Vilnius PS.

The C1M506 is much broader and includes the C1M515 passband region. The combination of both provides an index that is almost reddening free and its combination with the contiguous pseudo-continuum passbands (C1M467 and C1M549) provides an index sensitive to Mg abundances and gravity. If the luminosity is known from parallax, Mg abundances can be determined. The Ca II and Mg I spectral features show inverse behaviour when  $[M/H]$  and  $[\alpha/Fe]$  change (Tautvaišienė & Edvardsson 2002), and hence, indices using C1M395 and C1M515 allow the disentangling of Fe and  $\alpha$ -process element abundances.

The narrow passband C1M656 is placed on the  $H\alpha$  line. As mentioned in Section 5.1, the  $H\alpha = \text{C1B655–C1M656}$  index is a

measure of the intensity of the  $H\alpha$  line, yielding luminosities for stars earlier than A0 and temperatures for stars later than A3. The index is most useful for identification of emission-line stars (Be, Oe, Of, T Tau, Herbig Ae/Be, etc.).

C1M716 coincides with one of the deepest TiO absorption bands with a head at 713 nm (Wahlgren, Lundqvist & Kučinskas 2005), while C1M747 measures a portion of the spectrum where the absorption by TiO bands is minimum. So, the index C1M716–C1M747 is a strong indicator of the presence and intensity of TiO, which depends on temperature and TiO abundance for late K- and M-type stars. For earlier type stars, both passbands provide measurements of the pseudo-continuum. Earlier PS proposals for MBP considered the inclusion of a filter centred on the TiO absorption band at 781 nm. FoM computations and analysis of the  $\sigma_{k,\text{post}}$  values showed that the AP determination improves by more than 10 per cent, for [Ti/H] and  $T_{\text{eff}}$ , if the passband is centred on 716 nm instead of on 781 nm. A similar but narrower passband has been used in the Wing eight-colour far-red system.

The passband C1M825 is designed to measure either the continuum bluewards of the Paschen jump (hence its limitation at 842 nm for the red side mid-transmission wavelength) or the strong Carbon-Nitrogen (CN) band for R- and N-type stars. For M stars, C1M825 measures a spectral domain with weak absorption by TiO. The distinction between M and C stars is realized with all red passbands. At a given temperature, the fluxes are similar in the C1M747 and C1M861 for O-rich stars (the M sequence) and for C-rich stars (the C sequence), but very different in the C1M825 and C1M965 passbands, namely because of strong CN bands developing redwards of 787 nm. The separation between M and C stars is possible even if they are heavily reddened.

Similarly, C1M965 measures the continuum redwards of Paschen jump (and in combination with C1M825 yields the height of the jump) or strong absorption bands for R- and N-type stars (see Fig. 9, bottom). Having a passband at these very red wavelengths at the edge of the CCD QE curve improves the interstellar extinction determination, which was proven through the FoM computations.

The C1M861 passband, in between C1M825 and C1M965, is constrained by the wavelength range of the RVS instrument (i.e. 848–874 nm) and hence includes the Ca infrared triplet. The measurement of the flux of the star in this passband will help the RVS data reduction. The index C1M861–C1M965 measures the gravity-sensitive absorption of the high member lines of the Paschen series.

Finally, the indices C1M825–C1M861 and C1M861–C1M965 are a sensitive criterion for the separation of M-, R- and N-type stars (see Fig. 9, bottom).

## 6 PHOTOMETRIC PRECISION

This section describes the simulation of photometric fluxes that will be measured by *Gaia*, the associated magnitude errors and the effect on these errors of crowded regions and the calibration of the photometric measurements.

### 6.1 Simulated photometry

For the simulation of synthetic white light ( $G$ ,  $GS$ ), C1B and C1M fluxes and their corresponding errors, a photometry simulator GAIPHOTSIM<sup>4</sup> was created. This tool predicts the number of photoelectrons per unit time (or per CCD crossing) for every given

passband, observed target and *Gaia* instrument specification. GAIPHOTSIM also estimates the associated magnitude and the magnitude error per transit and at the end of the mission. The inputs are: the instrument parameters; the SED (from an empirical or synthetic spectral library) of the observed object; its apparent magnitude and radial velocity; the extinction law and the  $A_V$  value; the brightness of the sky background; and, optionally, the coordinates of the object on the sky. The coordinates allow the derivation of the actual number of observations according to the nominal scanning law. The adopted interstellar extinction law is that of Cardelli, Clayton & Mathis (1989) and the ratio of total to selective absorption can be chosen. The latter has a default value of 3.1. Simulations can be done for single and multiple stars, emission-line stars, peculiar stars, Solar system objects, QSOs, etc., actually for any given SED.

To compute the object flux  $s_j$ , measured in a given photometric passband  $j$  and collected after a single CCD crossing, the following ingredients are needed: the object SED; the assumed interstellar extinction and the extinction law all resulting in  $N(\lambda)$  (in units of photon  $\text{m}^{-2} \text{s}^{-1} \text{nm}^{-1}$ ); the transmission profile of the passband  $T_j(\lambda)$ ; the telescope transmittance  $T(\lambda)$ ; the detector response  $Q(\lambda)$  (the CCD QE); the pupil area  $A$ ; and the single-CCD integration time  $\tau$ . The object flux is then given by:

$$s_j[e^-] = A\tau \int_{\lambda_{\text{min},j}}^{\lambda_{\text{max},j}} d\lambda N(\lambda)T(\lambda)T_j(\lambda)Q(\lambda). \quad (1)$$

The flux  $s_j$  is converted into standard magnitudes  $m_j$  using the absolute flux calibration of Vega (Mégessier 1995), with all its colours set equal to zero. The SED of Vega has been modelled according to Bessell, Castelli & Plez (1998; a Kurucz SED of  $T_{\text{eff}} = 9550 \text{ K}$ ,  $\log g = 3.95$ ,  $[M/H] = -0.5$ ).

By default, the magnitude of the sky background is assumed to be at the level of the zodiacal light measured in *HST* observations and is set to  $V = 22.5 \text{ mag arcsec}^{-2}$ . This assumption is very conservative for most of the sky. For example, *HST* measurements show that the sky background is  $V = 23.3 \text{ mag arcsec}^{-2}$  at high ecliptic latitudes.

All simulations in this paper were run with the mean value for the total number of observations (see Table 1) and with the default values for the extinction law and the sky background.

### 6.2 Aperture photometry and associated errors

As discussed in Section 2.3, during the observational process only the pixels in the area immediately surrounding the target source are sent to the ground in the form of a ‘window’. In most cases, the pixels in the window are binned in the across-scan direction so that the resulting data consists of a 1D set of number counts per sample. Following an ‘aperture photometry’ approach, it is assumed that the object flux  $s_j$  within a given passband  $j$  is measured in a rectangular ‘aperture’ of  $n_s$  samples within the window. Some light loss can be produced due to vignetting and/or the finite extent of the ‘aperture’. Hence, the actual measured flux will be  $f_{\text{aper}} \times s_j$ , where  $f_{\text{aper}} \leq 1$ .

The end-of-mission magnitude error ( $\sigma_{m,j}$ ) is computed taking into account:

- (i) the total detection noise per sample  $r$ , which includes the detector readout noise;
- (ii) the sky background contribution  $b_j$  assumed to be derived from  $n_b$  background samples;
- (iii) the contribution of the calibration error per elementary observation  $\sigma_{\text{cal}}$ ; and
- (iv) the mean total number of observations  $n_{\text{eff}} = n_{\text{obs}} \times n_{\text{strips}}$ .

<sup>4</sup> A web interface is available at <http://gaia.am.ub.es/PWG/>

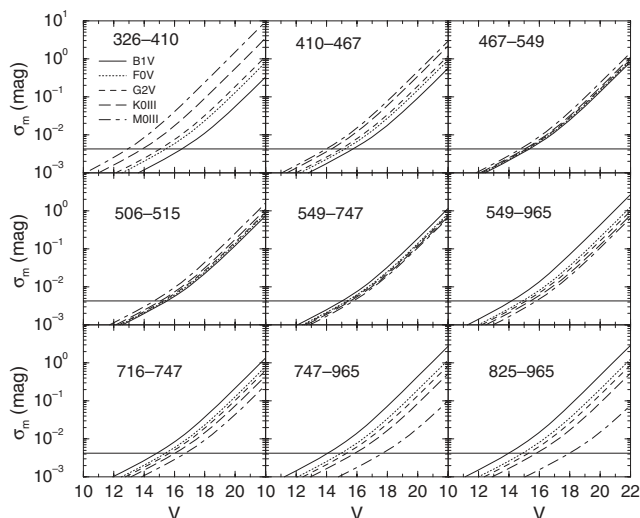


**Figure 10.** Estimation of the end-of-mission precisions as a function of  $V$  for several photometric indices constructed from the passbands in C1M and computed according to equation (2) with  $\sigma_{\text{cal}} = 0$  mag. In this paper, the contribution of the calibration error to the end-of-mission precision is estimated to be of 3 mmag in every passband. This is indicated by the horizontal line (which here includes a factor of  $\sqrt{2}$ ).

The resulting magnitude errors are increased by a 20 per cent ( $m = 1.2$ ) ‘safety margin’ to account for sources of error not considered here (such as a dependence of the calibration error on sky density and source brightness, see below):

$$\sigma_{m,j}[\text{mag}] = m \frac{1}{\sqrt{n_{\text{eff}}}} \left[ \sigma_{\text{cal}}^2 + \left\{ 2.5 \log_{10} e \times \frac{[f_{\text{aper}} S_j + (b_j + r^2) n_s (1 + n_s/n_b)]^{1/2}}{f_{\text{aper}} S_j} \right\}^2 \right]^{1/2}. \quad (2)$$

The attainable precisions are shown in Figs 4 and 6 where the estimated  $\sigma_{m,j}$  are plotted as a function of  $V$  and spectral type for the  $G$  and C1B passbands, respectively. The associated end-of-mission errors for several colour indices formed with the C1M passbands are shown in Fig. 10. A precision of 0.01 mag is obtained at  $V \sim 18$  and 16 for the BBP and MBP passbands, respectively.

For high S/N, the end-of-mission magnitude error is limited by  $\sigma_{\text{cal}}$ . Following the approach in the *Gaia* Study Report (ESA 2000, p. 264) and evaluating the number of involved calibration parameters and the number of available stars for calibration purposes,  $\sigma_{\text{cal}}$  ranges from 0.3 to 2 mmag depending on the instrument and the passband. Thus, potentially submillimagnitude photometric precisions can be achieved at the end of the mission. However, because there is no detailed calibration model for the photometric data processing at the moment, we prefer to be very conservative and we assume an ad hoc calibration error floor of 30 mmag per single observation, yielding a minimum calibration error of about 3 mmag at the end of the mission ( $\sigma_{m,j} \geq 3$  mmag).

### 6.3 Crowded areas, image restoration

An important limiting factor for the photometric accuracy is the distribution of the background flux around each source. Part of the background consists of diffuse emission from the general sky background and zodiacal light. In addition, there will be discrete background sources which may be fainter than the *Gaia* survey limit

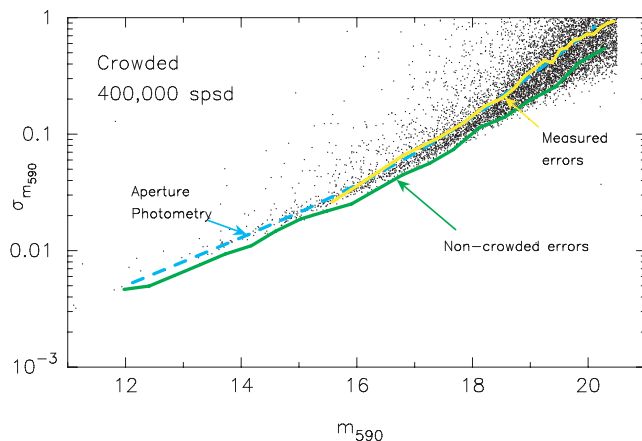


**Figure 11.** Various single transit error estimates: the dashed (blue) line is for the case of aperture photometry (equation 2); the solid (green) line for the case of PSF fitting photometry using accurate positional information from astrometric processing in a non-crowded field; and the shorter (yellow) line on the right above the green line shows the same for a crowded-field (400 000 stars  $\text{deg}^{-2}$ ). The black dots are the formal errors from the PSF fitting solution in the crowded case. ( $m_{590}$  is the magnitude for a representative MBP passband at 590 nm.)

( $G_{\text{lim}}$ ) and the point spread function (PSF) features of neighbouring bright stars may also contribute to the background. In Astro, there is the added complication that the fields of view from two telescopes overlap on the focal plane and that the two overlapping fields will be different for different scan directions.

This background problem becomes particularly severe in the more crowded areas on the sky (above  $\sim 10^5$  stars  $\text{deg}^{-2}$ ) where the limited resolution of the MBP instrument will lead to blending of sources in addition to the effects mentioned above. In this case, the data reduction will require a careful deconvolution and it was shown by Evans (2004) that this is possible for densities up to about  $2\text{--}4 \times 10^5$  stars  $\text{deg}^{-2}$  to 20 mag, by using the accurate positional information from the astrometric processing and the knowledge of the PSF in Spectro. Moreover, the study also showed that the precisions estimated from equation (2) are pessimistic (see Fig. 11). In non-crowded regions, PSF photometry yields lower errors than those estimated with aperture photometry.

The data processing for crowded regions can be improved further if we also have knowledge of disturbing sources around each object to a magnitude limit that goes fainter than  $G_{\text{lim}}$ . Images providing this knowledge can in principle be reconstructed from windows that were obtained for different scan directions. This reconstruction process has been studied by Dollet, Bijaoui & Mignard (2005) and Nurmi (2005) who present two different image restoration methods. Both studies show that, by combining the Astro sky mapper windows or a longer window in the Astro field, one can obtain images at a resolution of  $\sim 0.1\text{--}0.2$  arcsec that go 2–3 mag deeper than  $G_{\text{lim}}$ . Nurmi (2005) in particular shows that, using a longer AF window, one can map the disturbing sources in the immediate surroundings of objects (within a  $\sim 2.5$ -arcsec diameter) to  $V \sim 24$  for brightness differences  $\Delta V < 8$ . The image reconstruction will obviously also be useful in identifying components of multiple stars.

### 6.4 Calibration

The photometric precision and accuracy will ultimately be limited by how accurately the data are calibrated. At an elementary level,

the goal of the photometric data reduction is to accurately extract from each CCD image the object number counts and to transform these into calibrated fluxes on a standard scale.

The effects that influence the measured flux can be broadly divided into four categories:

- (i) the mirror and filter reflectivity and transmission profiles;
- (ii) the details of the CCD response, including non-linearities and charge transfer inefficiency effects;
- (iii) the point spread function and uneven image motion during the transit; and
- (iv) the sky background and disturbance from neighbouring sources.

The calibration process concerns the careful control and monitoring of these effects, all of which are time dependent.

The *Gaia* observations are fully self-calibrated and need not rely on any extant PS. The variations in response across the focal plane and the variations with time will be monitored and corrected taking advantage of the scanning mode in which *Gaia* will be operated. For average stellar densities on the sky, about 60 and 300 stars per CCD per second will cross the focal planes of Astro and Spectro, respectively. This translates to about 660 and 3400 stars per pixel column per 6 h (which is the spin period of *Gaia*). The same stars are observed repeatedly in different parts of the focal plane on time-scales varying from hours to weeks to months, up to the mission lifetime of 5 yr. Thus, there will be plenty of measurements to perform detailed CCD calibrations on scales from pixel columns to CCDs.

The PS will be defined by the average response for all the CCDs over the duration of the mission. It is also important to establish a standard scale, where all non-linearities in the response are corrected. These effects will be seen as magnitude-dependent PSFs, especially for the brighter sources. A more extensive discussion of the calibration issues for the photometric data processing can be found in Brown (2005).

## 7 PHOTOMETRY PERFORMANCES

The role of the PS is to astrophysically characterize the observed objects and, mainly, to determine APs for single stars. Thus, prior to parametrization, a classification is needed. Classification allows the identification of several kinds of objects (stars, QSOs, etc.). This is done mostly using the photometry, although parallaxes and proper motions will help the identification of extragalactic objects. Stellar parametrization with *Gaia* is very challenging due to the large range of stellar types (across the whole HR diagram) encountered, the complete absence of prior information and, for the vast majority of stars, the availability of only the 19 BBP and MBP fluxes. For some 100–200 million stars, parallaxes will be measured at the 10 per cent accuracy level. For the brightest stars, the RVS spectra will also provide information on APs. Parallaxes and the RVS will be used when available, although optimal exploitation of heterogeneous data requires sophisticated approaches. Other challenges are presented by: the presence of degeneracies (where, for example, a set of fluxes may correspond to more than one type of star, see also Section 4.5); the very large cosmic variance compared with limited data; the inevitable presence of strange objects; and the problem of accurately determining ‘weak’ APs ( $[M/H]$ ,  $\log g$ ) in the presence of dominant variance from ‘strong’ APs ( $T_{\text{eff}}$ ,  $A_V$ ).

This section presents two different evaluations of the performance of the *Gaia* PS with respect to the determination of APs for single stars. One approach is through the analysis of the posterior errors introduced in Section 4.2, taking into account photometry and par-

allax information. The other approach is through the analysis of results obtained with parametrization algorithms specifically designed for the AP determination. In both cases, we assume that the differences among the measured fluxes of the stars and, hence, the changes in their spectra are only due to differences of the AP  $p_k$  and the errors. We also assume that the SEDs and their change as a function of the parameters  $p_k$  match the true stars. In other words, cosmic dispersion (the effects of rotational velocity, magnetic fields, element-to-element chemical composition differences, differences in the interstellar extinction law, unresolved binarity and so on) and inaccuracies in the SED libraries [absence of chromospheres and some opacity sources, non-local thermodynamic equilibrium (NLTE) effects, simplified geometry, etc.] are not taken into account. In addition, for both approaches, we assume that the noise model described in Section 6.2 is correct. Therefore, both the posterior errors as well as the errors estimated from the parametrization algorithms are, in principle, optimistic. The posterior errors, which evaluate locally the sensitivity of the PS with respect to APs, are more optimistic than the results from the parametrization algorithms because global degeneracies are assumed not to exist (see Section 4.5). On the other hand, the errors on the APs estimated from the parametrization algorithms reflect a combination of the capabilities of the PS and of the algorithms themselves. Thus, a large estimated error may mean a poor PS performance or a poor efficiency of the algorithm, or both. The parametrization algorithm discussed in Section 7.2 only considers the C1M passbands: information from BBP and parallax is not included. Hence, the estimated errors tend to be pessimistic.

By the end of the *Gaia* mission, improved stellar atmosphere models, improved opacity sources, improved treatment of convective atmospheres, dusty atmospheres, geometry, NLTE effects, etc. will be available. This, supplemented with real data where appropriate, will allow us to minimize one source of inaccuracies.

### 7.1 Posterior error, $\sigma_{k,\text{post}}$ , estimations

The posterior errors on the APs,  $\sigma_{k,\text{post}}$ , for the baseline C1B and C1M PS have been computed as explained in Appendix A and are presented here. The targets from Section 4.3 have been grouped by spectral type, luminosity class and Galactic direction, and their mean  $\sigma_{T_{\text{eff}},\text{post}}/T_{\text{eff}}$ ,  $\sigma_{A_V,\text{post}}$ ,  $\sigma_{\log g,\text{post}}$  and  $\sigma_{[M/H],\text{post}}$  are shown in Fig. 12 as a function of distance from the Sun (i.e. as a function of apparent magnitude). The figure shows the error predictions based on the BaSeL 2.2 SED library and the combination of the white light, BBP and MBP fluxes with parallax information. The fluxes measured in the different passbands are assumed to vary only due to changes in  $T_{\text{eff}}$ ,  $A_V$ ,  $\log g$  and  $[M/H]$ . Using other SED libraries leads to slightly, but not significantly, different  $\sigma_{k,\text{post}}$  values. The largest differences occur for cool stars ( $\lesssim 4000$  K) for which the differences among synthetic spectral libraries are large. For these stars, discrepancies among theory and observations also exist. See Kučinskas et al. (2005) for a comparison of observed colour indices and predictions by the PHOENIX, MARCS and ATLAS model atmosphere codes for late-type giants.

For a given group of spectral types and luminosity classes, the posterior errors increase with the distance to the Sun, because the stars become fainter and the measurement errors of their fluxes increase. In the Galactic plane, the stars are also increasingly reddened (and fainter) with distance, which also leads to larger errors. Given a distance and a group, the posterior errors increase from the Galactic pole direction to the Galactic centre direction due to the increase of interstellar extinction. For a given distance and direction, the

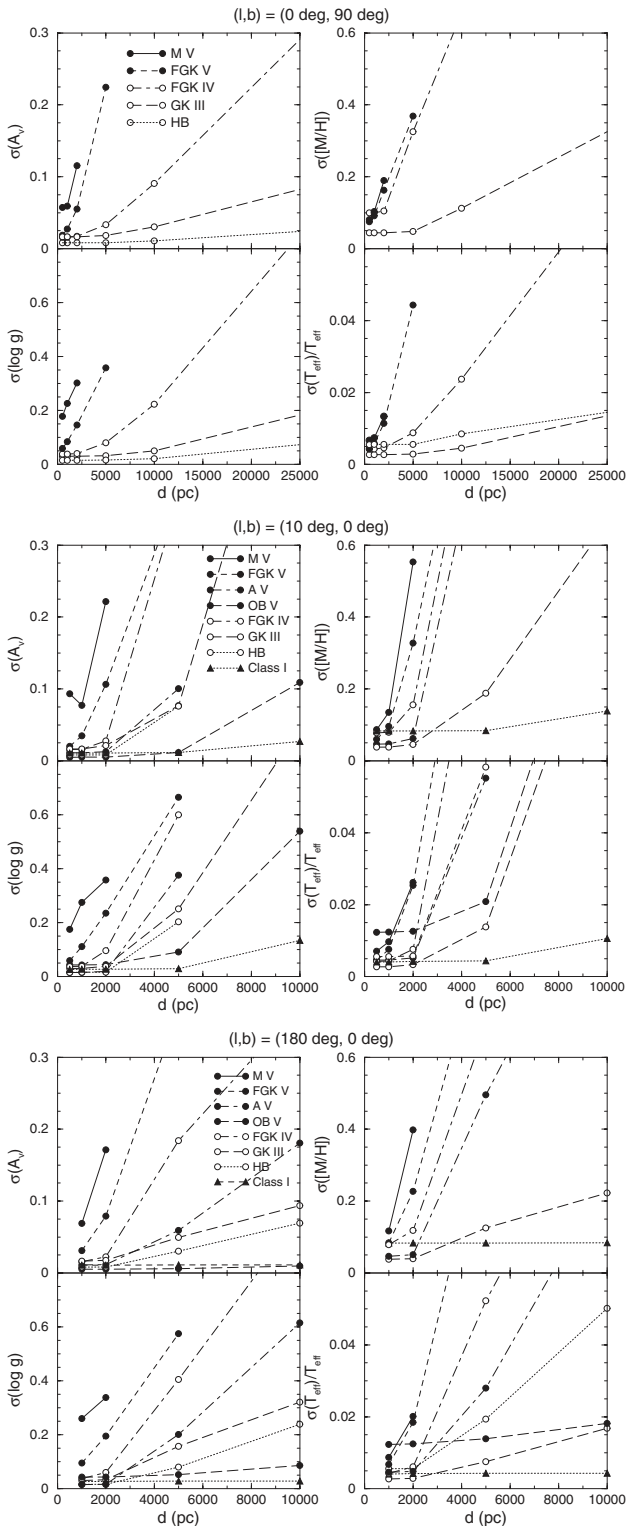


**Figure 12.** Predicted (posterior) errors for the main astrophysical parameters in three Galactic directions based on  $G$ , C1B, C1M and parallax data. The following assumption holds for  $A_V$ : in the Galactic pole direction it reaches 0.3 mag at 1 kpc and is constant from this distance onwards; towards the Galactic centre it ranges from 0.3 mag at 500 pc to 10 mag at 10 kpc; and towards the anticentre it varies from 0.3 mag at 500 pc to 3.5 mag at 5 kpc and is constant for large distances. The figure legends indicate the meaning of the lines, where ‘Class I’ means luminosity class I and ‘HB’ means horizontal branch stars.

errors are larger for dwarfs than for giants and supergiants due to the different absolute magnitudes.

The lower limit on the  $\sigma_{k,\text{post}}$  values reflects the minimum photometric error due to the contribution of calibration errors. As discussed in Section 6.4, we have conservatively assumed an ad hoc error floor of  $\sim 3$  mmag at the end of the mission.

Bulge stars are generally faint because of their distance and the high extinction towards them. However, there are areas of low extinction, such as Baade’s window, but there the stellar density is very high and MBP measurements will not be available. In those cases, the derived stellar parameters, based only on  $G$ , BBP photometry and parallaxes, are less precise. Nevertheless, the estimated  $\sigma_{A_V,\text{post}}$  ranges from 0.2 to 0.6 mag,  $\sigma_{T_{\text{eff},\text{post}}}/T_{\text{eff}}$  from 1 to 10 per cent and  $\sigma_{\log g,\text{post}}$  from 0.1 to 0.5 dex, depending on the spectral type. In the high extinction areas, the lower stellar densities allow for MBP measurements and, even though the stars are very faint, the estimated precision of the APs is still acceptable:  $\sigma_{A_V,\text{post}}$  ranges from 0.4 to 1.0 mag,  $\sigma_{T_{\text{eff},\text{post}}}/T_{\text{eff}}$  from 2 to 15 per cent and  $\sigma_{\log g,\text{post}}$  from 0.3 to 0.7 dex.

Fig. 13 shows the  $\sigma_{k,\text{post}}$  values as a function of apparent  $G$  magnitude and  $[M/H]$  for F-type stars representative of isochrone turn-offs for the old-disc, thick-disc and halo stars. This example has been chosen because F-type stars at the turn-off are key targets for many Galactic topics (see Table 2). The performance of the PS is excellent up to about  $G = 18$ , even for the most metal-poor stars, and

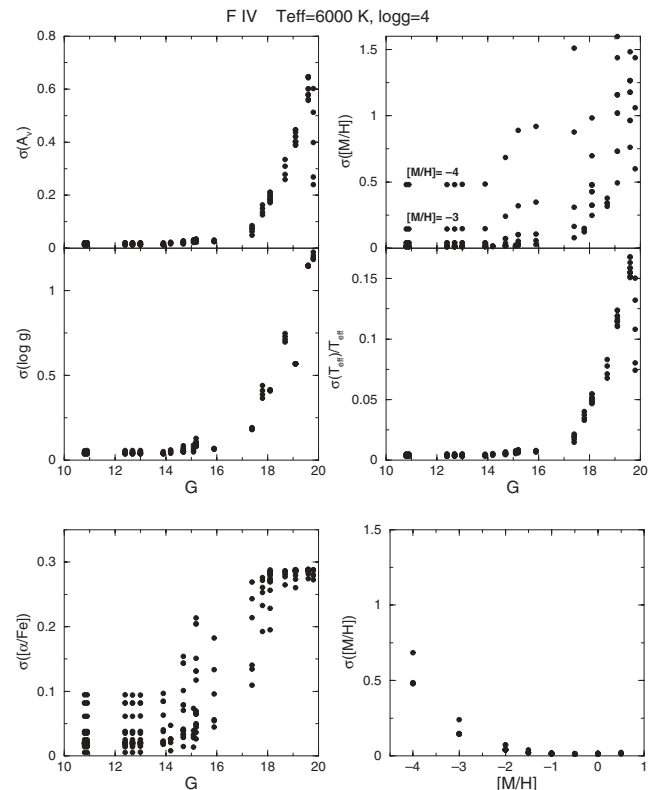


**Figure 13.** Predicted (posterior) errors for the astrophysical parameters as a function of apparent  $G$  magnitude and  $[M/H]$  for F-type subgiants. The top four panels show the results based on the BaSeL 2.2 SED library. In the top right panel, the metallicity increases from  $[M/H] = -4$  at the top to  $[M/H] = +0.5$  at the bottom for each vertical set of dots. The bottom left panel shows the predicted errors for  $[\alpha/\text{Fe}]$  based on the NEXTGEN 2 SED library. The bottom right panel shows the error on  $[M/H]$  as a function of  $[M/H]$  for stars brighter than  $G = 15$  (based on BaSeL 2.2 SEDs).



decreases for faint magnitudes. The determination of  $[\alpha/\text{Fe}]$  is only possible up to  $G \approx 16$ , while at  $G \approx 18$ , the measurement errors are large enough to make the changes in SEDs indistinguishable, which means that  $\sigma_{[\alpha/\text{Fe}],\text{post}} \sim \sigma_{[\alpha/\text{Fe}],\text{prior}} = 0.3$  dex.

As discussed in the introduction of this section, the  $\sigma_{k,\text{post}}$  values are optimistic by construction and, from the figures above, they may seem too optimistic compared with the achievable precisions with the currently available PSs. However, they are not necessarily overly optimistic. *Gaia* photometry will provide measurements in five broad and 14 medium passbands and the *G* white light passband, to which the information contained in the parallaxes can be added. There is no precedent for deriving stellar APs in this way.

The  $\sigma_{k,\text{post}}$  here represent the maximum precision that can be obtained. We estimate that the main uncertainty on the actual values comes from the imperfect knowledge of the SEDs of the true stars and not from the design of the PS itself.

## 7.2 Estimating the astrophysical parameters

The predicted errors discussed above are evaluated locally and hence they are based on the assumption that global degeneracies (e.g. the confusion between a reddened hot star and an unreddened cool dwarf) are already accounted for before the APs are estimated. We now discuss the performance of the *Gaia* PS in a more realistic setting where the APs of each source have to be derived from the measured photometry in the presence of global degeneracies.

### 7.2.1 Methods for astrophysical parametrization

Numerous statistical methods are available for estimating parameters from multidimensional data. The most appropriate are supervised pattern recognition methods, which involve a comparison of the observed ‘spectrum’ (the set of observed filter fluxes) with a set of template spectra with known APs (the ‘training grid’).

Minimum distance methods (MDMs) make an explicit comparison with every spectrum in the training grid to find the ‘closest’ match according to some distance metric (e.g. Katz et al. 1998). Because only discrete APs of templates in the training grid can be assigned to the observed spectrum, the precision is limited by the ‘AP resolution’ in the grid. This may be partially alleviated by averaging over the APs of the nearest neighbours or by interpolating between them (e.g. Bridžius & Vanevičius 2002; Malyuto 2005).

Instead of making an explicit comparison with every template spectrum, we can model the mapping between the observed data space,  $\mathcal{D}$ , and the AP space,  $\mathcal{S}$ , with a regression function  $p = f(\phi; w)$ , i.e. the AP  $p$  are a function of the fluxes  $\phi$  and a set of free parameters  $w$ . We then solve for the free parameters  $w$  via a numerical minimization of the errors in the predicted APs of the training data. As both  $\mathcal{D}$  and  $\mathcal{S}$  are multidimensional and because  $\mathcal{D} \rightarrow \mathcal{S}$  is an inverse mapping (and hence may show degeneracies), the problem is complex (Bailer-Jones 2003, 2005). None the less, it offers advantages over the direct template matching, such as less dependence on a dense template grid, provides continuous AP estimates and provides much faster application times to new data (because the mapping function is learned in advance). There are many ways to implement a multidimensional regression, including neural networks (NNs) and adaptive splines (see e.g. Hastie, Tibshirani & Friedman 2001).

Various methods have been tested by the *Gaia* classification and photometry working groups and each have their advantages and disadvantages. For more details, see Brown (2003). In the rest of this section, we focus on one particular method. It must be stressed

that this is just a preliminary investigation into AP estimation with *Gaia* and is restricted to just the C1M passbands.

### 7.2.2 A regression model

We applied a feed-forward NN to a set of simulated photometry in the medium-band C1M component of the *Gaia* PS. The training grid consists of 61 941 simulated ‘spectra’ showing variance in the four AP  $T_{\text{eff}}$  (2000 to 50 000 K),  $[\text{M}/\text{H}]$  ( $-5.0$  to  $+1.0$ ),  $\log g$  ( $-1.0$  to  $+5.5$ ),  $A_V$  and the line-of-sight interstellar extinction (0.0 to  $+5.0$ ). The source spectra were taken from the BaSeL 2.2 library. The distribution over the APs is discretized and non-uniform (Fig. 14, right panel). We used the STATNET NN code (Bailer-Jones 1998, 2000) with two hidden layers each comprising 25 hidden nodes. STATNET is trained with a conjugate gradient optimizer with weight decay regularization to avoid overfitting. We assess the performance by applying the network to a separate set of data: the distribution of the APs in this ‘test set’ is shown in Fig. 14 (left panel). In total, there are 9229 different stars (AP combinations) in the test set, each represented by 10 different noisy passband fluxes for a given magnitude. Separate models were trained and tested at magnitudes  $G = 15, 18$  and  $20$ , i.e. with the appropriate amount of simulated noise, from which we can assess performance as a function of magnitude. All combinations of individual values of the four APs and the apparent  $G$  magnitude have been used without regard to the reality of such combinations. Moreover, we do not build in any prior information concerning the probability of occurrence of the various AP combinations.

### 7.2.3 Results

The results are summarized in terms of the average absolute errors

$$E = \frac{1}{N} \sum_{p=1}^N |\text{computed}(p) - \text{true}(p)|, \quad (3)$$

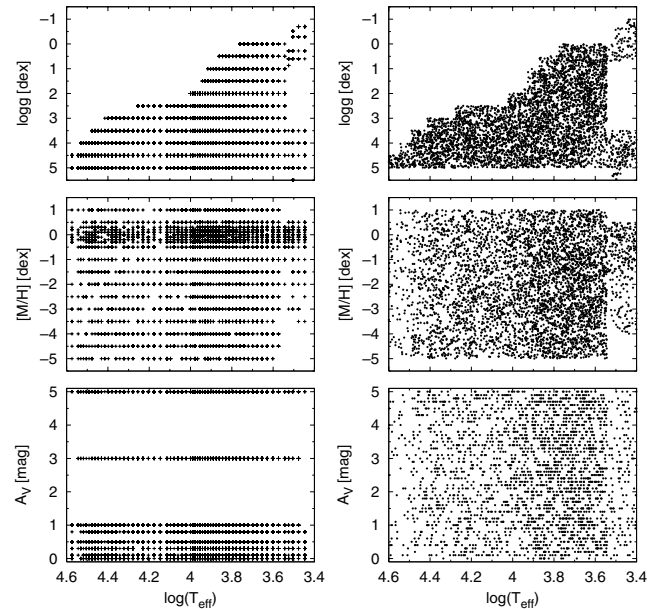


**Figure 14.** The distribution of the astrophysical parameters in the training (right) and test set (left). In total, there are 61 941 stars (AP combinations) in the training set and 9229 different stars (each represented by 10 different noisy filter fluxes for a given magnitude) in the test set.

where  $p$  denotes the  $p$ th spectrum (star) and  $\text{computed}(p)$  is the parametrization output provided by the network. The errors for  $T_{\text{eff}}$  are given as the fractional errors. It is well known that the error in any AP for a given star depends significantly not only on the value of that AP, but also on the value of the other APs. Therefore, reporting a single error for each AP by averaging over the full range of the other APs has little meaning and also depends strongly on the AP distribution in the test set. We therefore present errors averaged over selected narrow ranges of APs. This is only for reporting purposes. When the network is presented with a star to classify, it has no prior knowledge of its APs (not even that it is restricted to the range in the training set).

Representative plots of the AP errors are shown in Fig. 15 for  $G = 15$ . This plot is for dwarf stars, i.e.  $\log g \in [3.5, 5.5]$  dex, although the results are not significantly different for giants. A complete overview of the results for all stellar types is given in Willemsen, Kaempf & Bailer-Jones (2005a).

For hotter stars (A- and B-type stars) the errors in  $[M/H]$  and  $T_{\text{eff}}$  are larger than those for cooler stars (G and K type), while the  $A_V$  and  $\log g$  errors are smaller. This behaviour is expected and reflects what we know of how the APs are expressed in the SED as a function of the APs (in particular  $T_{\text{eff}}$ ). For stars of G type and earlier, the extinction is determined quite well. For example, for A stars, we find errors of 0.03 to 0.06 mag for  $G = 15$  and 0.07 to 0.15 mag for  $G = 18$  mag. For cooler stars (K and M), the performance degrades slightly, especially for highly extinct cool stars.

Metallicity determinations are possible for cool and intermediate-temperature objects (M to F type) with precisions ranging from 0.1 to 0.4 dex, even at low metallicities. For the same stars,  $[M/H]$  can be determined to 0.1–0.2 dex down to  $-2$  dex metallicity. Here, only stars with  $T_{\text{eff}} \geq 3500$  K have been included. For stars below  $\sim 4000$  K, the estimated uncertainties may be unrealistic due to the

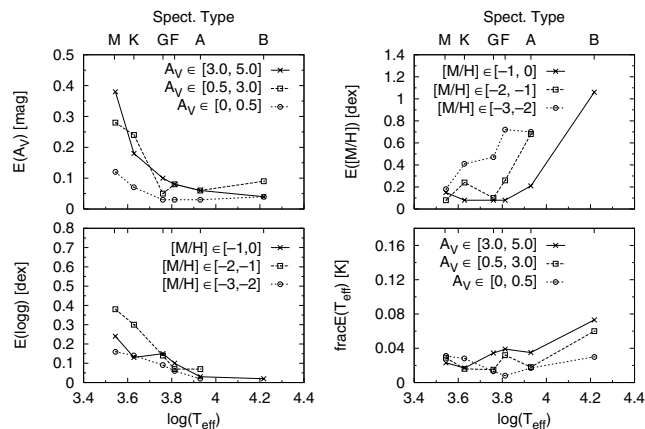


**Figure 15.** Parametrization errors (as defined in equation 3) for the four astrophysical parameters (APs) as a function of  $T_{\text{eff}}$  for different subsets of  $A_V$  and  $[M/H]$ . For a given  $T_{\text{eff}}$ , a data point lies at the average of a representative temperature interval. Other than for the  $\log g$  error plot, results are shown averaged over the range  $\log g \in [3.5, 5.5]$  dex, although the results are not significantly different for giants. For  $A_V$  and  $T_{\text{eff}}$ , the results are shown for  $[M/H] \in [-1, 0]$  dex; for metallicity and gravity,  $A_V$  is limited to  $[0, 0.5]$  mag. The errors for  $T_{\text{eff}}$  are the fractional errors. While we show results for these limited AP ranges for clarity, it is important to realize that the model was trained and tested on the full range of APs shown in Fig. 14: there was no prior restriction on the APs of a star presented to the model, even though several combinations of  $G$  and APs may not exist in the Galaxy. All results for the C1M passbands for stars at  $G = 15$  mag using simulated photon fluxes are representative of the end of the mission.

inaccuracies of the current atmosphere models, which in this work are assumed to match the reality, as discussed previously.

The precision of the gravity determination depends on the temperature, but is basically independent of metallicity. We find errors of  $E(\log g) = 0.08$  to  $0.4$  dex for these stars at  $G = 15$  mag and  $0.2$  to  $\sim 1.0$  dex at  $G = 18$  mag. For hot stars (A and B type), we find errors of  $\sim 0.1$  dex or better, even for  $G = 18$  mag. This will provide good discrimination between distant halo HB stars and nearer A dwarfs in those cases where the parallaxes are poor.

Temperatures can be determined to between 1 and 5 per cent for M- to A-type stars ( $G = 15$  mag) and to precisions of 2 to 11 per cent at  $G = 18$  mag. There is some dependence on the extinction. For lower values of the extinction ( $A_V \in [0, 0.5]$  mag), we find temperature errors of  $E(T_{\text{eff}}) \leq 4$  per cent for ( $G = 15$ ) and  $\leq 5$  per cent ( $G = 18$ ) for all types of stars.

We performed additional tests to determine the  $[\alpha/Fe]$  abundance using the NEXTGEN 2 SED library. This increases the dimensionality of the AP space (from four to five) and thus its complexity. We used the same NN approach and the C1M passbands. We found errors of  $E([\alpha/Fe]) \sim 0.1$  dex for low- to intermediate-temperature stars at  $G = 15$  mag. Our results also suggest that precisions of 0.2 dex should be possible for  $G \lesssim 16.5$  mag. See Willemsen & Bailer-Jones (2005) for more details.

Comparative tests were also made with MDM and Radial Basis Function Neural Networks (RBFNNs) using the same data. In general, feed-forward NNs yielded the best results, followed by MDM and then RBFNN.

### 7.3 Discussion

These preliminary results, based on the C1M passbands, demonstrate that an automated ‘bulk’ determination of APs is possible.

The posterior errors predicted from the sensitivity of the SEDs to changes in APs are lower than the errors estimated from the NN results because the former are immune to global degeneracies (by design), whereas the NN performance is degraded by its failure to explicitly deal with degeneracies (which produce a non-uniqueness in the mapping it is trying to solve). The NN performance may be degraded by inefficiencies in the formulation of the problem via multidimensional regression. Yet, the posterior errors are based on C1B, C1M and parallax data, while the errors with the NN are estimated using only C1M passbands. Taking all into account, Figs 12, 13 and 15 show an overall agreement.

The actual set of training data we will use for the *Gaia* data processing will be based on improved stellar atmosphere models supplemented with real data. However, even then the training data are unlikely to represent the full range of cosmic variance in the APs that *Gaia* will encounter.

The performance predictions from the present implementation of the NN discussed above are pessimistic in several ways. First, only the C1M passbands were used. Including data from the five C1B passbands will improve the results (for instance, the index C1B655–C1M656 helps to break degeneracies among  $T_{\text{eff}}$ ,  $\log g$  and  $A_V$ ). Secondly, the use of the parallax, when available, will also help as it provides information on the intrinsic luminosity (for known apparent magnitude and estimated extinction), which will help solving degeneracies between  $\log g$  and chemical composition. Initial tests of including the parallax as an additional network input confirm that this improves the estimation of the gravity, especially for those stellar types for which  $\log g$  is otherwise poorly constrained (i.e. for intermediate- and low-temperature stars). It also improves the metallicity estimates (Willemsen et al. 2005b). This decrease

of global degeneracies makes the estimated errors from NNs more similar to the predicted posterior errors. Thirdly, for the brightest stars, the RVS provides high S/N spectra for all types of stars. This should improve the AP estimates. Finally and most importantly, we know that the method we have used is limited in a number of ways. For example, the AP mapping must be inferred based only on the training data. Explicitly providing information on the sensitivity of passbands or passband combinations to APs will help. Likewise, the NNs do not yet deal with AP degeneracy. This is a particular problem at low S/N. Overall, the predicted PS performances from Section 7.2 are rather conservative estimates of what will ultimately be possible with *Gaia*.

## 8 SCIENCE IMPLICATIONS

As emphasized a number of times, the main scientific goal of *Gaia* is the quantitative description of the chemical and dynamical evolution of the Galaxy over its entire volume. This is only possible if physical properties of stars, through chemical abundances and ages, are analysed together with kinematics and distances. To determine ages and abundances with an accuracy sufficient for Galactic studies, temperatures (and hence extinction) and luminosities have to be accurately determined as well.

In the following subsections, we outline the implications of the *Gaia* PS performance for addressing the science case. However, an in-depth discussion is not intended. In addition, we comment on the photometric performance for QSO classification. As mentioned in Sections 1 and 5.1.2, a proper identification of QSOs will allow the definition of a non-rotating extragalactic reference frame, which is indispensable for astrometric purposes. For other objects, we refer to Kaempf, Willemsen & Bailer-Jones (2005) who deal with the automatic parametrization of unresolved binary stars, to Kolka et al. (2005) for the study of performances for emission-line stars and to Cellino et al. (2005) for a discussion about *Gaia* photometry and the parametrization of asteroids.

### 8.1 Interstellar extinction and effective temperature

The determination of the effective temperatures, absolute magnitudes and chemical abundances requires accurate estimates of interstellar extinction including the interstellar extinction law. Ideally, the extinction estimates for individual stars are based solely on the observables of each star, as the extinction varies on small scales in any field except for the closest stars. Assuming a standard extinction law, the photometry of *Gaia* allows the determination of such individual extinction measures (see Figs 12, 13 and 15), though with significantly larger error for the late-type stars due to degeneracy in the  $A_V$  and  $T_{\text{eff}}$  determinations. Meanwhile, the determination of  $T_{\text{eff}}$  for the late-type main-sequence stars remains reliable, even in the presence of significant extinction, to at least  $G = 18$ . Effective temperatures with similar uncertainties are achievable for red giants in the halo where the extinction is low.

We can identify the main contributors to the determination of reddening. For example, the C1M825–C1M965 versus the C1B655–C1M656 ( $H\alpha$  index) diagram is useful for extinction measurements. The C1M825–C1M965 colour index is primarily meant as a measure of the strength of the Paschen jump, sensitive to stellar type, while the  $H\alpha$  index is nearly reddening free. For stars where the  $H\alpha$  index is a measure of the strength of the Balmer line, i.e. stars earlier than about G3–G5, the unreddened main-sequence displays a sharp locus in this colour–colour diagram. However, the same  $H\alpha$  index value may be measured for stars on either side of the Balmer maximum (A1–

A3 stars), but this ambiguity is lifted by comparison to the C1M656–C1M965 versus  $H\alpha$  index diagram. Thus, the inclusion of the  $H\alpha$  index allows a classical approach to determining intrinsic colours from standard curves and simultaneously correcting the colours for the influence of metallicity and evolution across the main sequence. However, again, intrinsic colours only result when the  $H\alpha$  index is measured precisely, while a potential drawback of the C1M825–C1M965 index is that these two C1M passbands are among those least affected by extinction.

If the reddening in only one colour index is determined, then the extinction in other passbands would have to rely on an assumed extinction law. Indeed, in our performance analysis (Section 7), we have assumed a standard extinction law. Deviations from this standard law (Fitzpatrick 1999), due to spatial variations in the chemical composition and size distributions of interstellar dust, will contribute to systematic errors in the individual extinction determinations. The breadth of the PS of *Gaia* justifies addressing the question of whether the extinction law itself (averaged over the line-of-sight to a star) can be determined from the photometry. Since *Gaia* is a comprehensive survey of all point sources, the number of sources is large enough that most stellar types are sufficiently represented even in small fields, close to the Galactic plane, where extinction correction is most essential. In this case, local extinction laws may possibly be deduced from colour difference versus colour diagrams. For example, deviant extinction laws may be identified from  $Q$ -like indices versus colour diagrams.

*Gaia* RVS observations will provide other measures of extinction. First, there is the diffuse interstellar band at 862 nm located within the wavelength range of the RVS instrument (Katz et al. 2004). In addition, the equivalent width of the IR calcium triplet gives a rough indication of the  $T_{\text{eff}}$ : in combination with the virtually reddening free C1M395–C1M410 index, the calcium triplet can be used as a diagnostic of intrinsic colours and thus to estimate the extinction. Together with *Gaia* parallaxes, all of these measures of extinction (spectroscopic and photometric) will allow the construction of a 3D Galactic extinction map.

*Gaia* measurements will also allow a statistical approach to the construction of a 3D extinction map. Given the parallax, main-sequence loci may be empirically constructed from nearby, unreddened samples provided by *Gaia*. Shifting these loci to a given distance with a given mean extinction identifies the main sequence in the observed colour–magnitude diagram (including the photometric errors) for a sample of main-sequence stars selected from a small volume element in the Galaxy. Thus, main-sequence fitting to such stellar samples, selected by means of the *Gaia* parallaxes, could serve as the basis for a 3D extinction map (Knude 2002). The chemical composition of the stars may be used to refine the definition of an appropriate main sequence, and  $\log g$  to refine the selection of an appropriate stellar sample. This approach has the further advantage that the C1B passbands may be used in addition to the C1M ones and that stars along the entire main sequence will contribute to the estimation of extinction, including those located on the lower main sequence where extinction determination is otherwise difficult.

The combination of *Gaia* and external IR photometric data provides independent determinations of extinction. During the luminosity calibration of Two-Micron All Sky Survey (2MASS) photometry for A9–G5 main-sequence stars, Knude & Fabricius (2003) noticed significant reddening vectors in the  $M_J$  versus  $(J - H)_{\text{obs}}$  diagram, where  $M_J$  was estimated from *Hipparcos* parallaxes  $\pi > 8.0$  mas and  $\sigma_\pi/\pi < 0.11$ , assuming that reddening was negligible. These vectors are most pronounced for the A-type stars but are also present for cooler ones. From these vectors, the extinction law may be

**Table 5.** Distances for which the relative parallax error is  $\sim 10$  per cent:  $d_0$  is the value of this distance for zero interstellar extinction and  $d_{\text{abs}}$  is the value for an average Galactic plane interstellar extinction of  $0.7 \text{ mag kpc}^{-1}$ .  $V(d_0)$  and  $V(d_{\text{abs}})$  are the corresponding apparent  $V$  magnitudes. Parallax accuracies are from table 8.4 in ESA (2000).

SP	$M_V$	$d_0(\text{pc})$	$V(d_0)$	$d_{\text{abs}}(\text{pc})$	$V(d_{\text{abs}})$	SP	$M_V$	$d_0(\text{pc})$	$V(d_0)$	$d_{\text{abs}}(\text{pc})$	$V(d_{\text{abs}})$
B1 V	-3.2	20 000	13.2	7000	15.7	G8 III	0.8	9000	15.6	4400	17.1
A0 V	0.65	8500	15.2	4500	16.8	K3 III	0.3	10 000	15.3	4800	17.1
A3 V	1.5	7000	15.7	3800	17.1	M0 III	-0.4	13 000	15.2	5500	17.2
A5 V	1.95	6500	16.0	3500	17.3	M7 III	-0.3	17 000	15.9	6300	18.1
F2 V	3.6	4500	16.7	2700	17.8						
F8 V	4.0	4000	17.0	2500	18.1	B0 Ib	-6.1	33 000	11.5	9500	15.4
G2 V	4.7	3500	17.2	2200	18.2						
K3 V	6.65	2400	18.4	1700	19.1	WD	8.0	1500	18.9	1200	19.2
M0 V	8.8	1500	19.7	1200	20.0						
M8 V	13.5	500	21.8	450	22.1						

estimated even for various spectral classes if the stellar density is large enough. Similar diagrams may be constructed from *Gaia* astrometry and BBP and MBP for the optical region and for the near-infrared from the 2MASS, UKIRT Infrared Deep Sky Survey, and the Visible and Infrared Survey Telescope for Astronomy (VISTA) surveys so that regions with abnormal extinction can be identified.

## 8.2 Absolute luminosity and gravity

Photometry will be crucial for absolute luminosity (or gravity) determination when relative parallax errors are larger than 10–20 per cent. The distances at which the relative parallax error is  $\sim 10$  per cent are listed in Table 5 as a function of spectral type and luminosity class in the absence of interstellar extinction, i.e. similar to the Galactic pole direction, and in the case of an average Galactic plane interstellar extinction of  $0.7 \text{ mag kpc}^{-1}$ . The parallax accuracies are from table 8.4 in the *Gaia* Study Report (ESA 2000). Based on the Besançon Galaxy model (Robin et al. 2003), some 100–200 million stars are predicted to have parallaxes measured at the 10 per cent accuracy level.

Absolute magnitude calibrations can be established, using the stars with accurate parallaxes and interstellar extinction, and applied to more distant stars in the classical way, assuming that these are intrinsically similar to the accurate-parallax stars, which may not always be the case. Thus luminosities with precision  $\sigma_{M_V} \sim 0.2\text{--}0.4 \text{ mag}$  (or  $\sigma_{\log g} \sim 0.1\text{--}0.2 \text{ dex}$ ) from photometry are desirable to match the uncertainties of the well measured parallaxes.

The main contributors to the photometric luminosity determination are the measurements of Balmer and Paschen jumps, the  $H\alpha$  index, the C1M395–C1M410 versus W(CaT\*) diagram and C1M515 combined with contiguous pseudo-continuum passbands, as already noted in Section 5.

Figs 12, 13, and 15 show that  $\sigma_{\log g} \sim 0.1\text{--}0.2 \text{ dex}$  is achievable for giants and early-type stars at large distances and therefore that the study of Galactic structure on large scales (warp, spiral arms, outer halo, etc.) is feasible. For nearby stars, the photometric determination of  $\log g$  is also possible but of less interest because of the good parallax precision. For distant late-type dwarf stars, i.e. with parallax errors larger than 10 per cent, the precision of the photometrically determined  $\log g$  will be not as good as for giants and early-type stars, as expected.

## 8.3 Chemical abundances

High-resolution, high S/N spectroscopic observations allow the most reliable chemical abundance determinations (e.g. Cayrel de

Strobel, Soubiran & Ralite 2001). RVS spectra will be used to determine the atmospheric parameters, when possible. Katz et al. (2004) estimate  $\sigma_{[M/H]}$  to be smaller than 0.2–0.3 dex for stars with  $V \sim 14$  and to improve by combining the spectra with photometric and astrometric data. Thus, atmospheric parameters for 10–25 million stars to  $V \sim 14\text{--}15$  will be determined including individual abundances for 2–5 million stars to  $V \sim 12\text{--}13$  (mainly Fe, Ca, Mg and Si for F–G–K stars; N in hotter stars, such as A-type stars; and information on C, N or TiO abundances for cool K- and M-type stars).

Although 10–25 million stars with RVS chemical abundance determinations may seem little compared with the 1 billion objects observed by *Gaia*, the spectroscopic chemical compositions are crucial as they will serve to calibrate the photometric data. This is important because, for the vast majority of stars, chemical abundances will be derived from photometric data exclusively.

The chemical abundances and especially the relation between  $[M/H]$  and  $[\alpha/Fe]$  are indicative of the initial star formation rate (SFR) and provide the rate of chemical enrichment of the Galaxy. Calculations by Maeder (2000) show that the  $\alpha$ -element abundance ratio starts to decrease at high  $[M/H]$  as the initial SFR increases. In agreement with this, Nissen (1999) argues that the thick-disc stars underwent chemical evolution with a high initial SFR such that a relatively high metallicity ( $[M/H] \sim -0.4$ ) was reached before the contribution by iron due to the Type Ia supernovae (SNe Ia) decreased the  $[\alpha/Fe]$  value. He also argues that the initial SFR in the thin disc has been slower and that the relative  $\alpha$ -element to iron abundances started to decrease at lower metallicity ( $[M/H] \sim -0.6$ ). Most of the halo stars were formed at an even lower initial SFR, so the decrease of  $[\alpha/Fe]$  occurs at low metallicity ( $[M/H] \sim -1.2$ ). Some of the halo stars have  $[\alpha/Fe]$  abundances typical of the thick disc, which points to a dual model for the halo formation: an inner part that had a high SFR and an outer part that experienced a slower evolution or was accreted from dwarf galaxies.

Figs 12, 13 and 15 show that *Gaia* photometry is able to match the expected spectroscopic precision up to about 1–2 kpc from the Sun depending on the Galactic direction (i.e. the reddening) for F–M dwarfs and subdwarfs. For giants in the red clump and the red giant branch, both being brighter, the same precision is attainable up to about 4, 7 and 12 kpc in the centre, anticentre and orthogonal Galactic directions, respectively. This implies that the following issues (and other goals) can be addressed: the determination of the Galactic chemical abundance gradient, the classification of the stars into different stellar populations, the characterization of halo streams

and the determination of the distance scale through the metallicity determination for RR Lyrae.

As expected, low metallicities are determined with less precision than solar or higher metallicities. Extensive spectroscopic follow-up efforts from the ground will be necessary to determine the metallicities of stars with  $[M/H] < -3.0$  with a sufficient accuracy to select the most interesting targets for high-resolution spectroscopy (Christlieb, private communication).

Photometric chemical composition determinations are not free of difficulties. For instance, cool unresolved binaries tend to mimic a single star with a lower metal content. As an example, for G and K dwarfs with companions for which  $\Delta m$  is 1.5–2 mag, the systematic metallicity error is  $\Delta[M/H] \sim -0.4$ . This bias decreases to  $\Delta[M/H] \sim -0.2$  when  $\Delta m = 3$ .

As discussed in Section 7, the first trials to determine  $[\alpha/Fe]$  using the NEXTGEN 2 library ( $[M/H] \in [-2, +0]$  and  $[\alpha/Fe] \in [-0.2, +0.8]$ ) show that precision of 0.1–0.2 dex for  $G \sim 15$ –16.5 can be achieved. The determination may be improved with the inclusion of parallax information, because it constrains the value of  $\log g$ , which may break the degeneracy in the variation of the Mg Ib triplet due to luminosity and Mg abundance changes. For stars fainter than  $G \sim 16$ –17, deriving  $\alpha$ -element abundances from photometry is unlikely.

#### 8.4 Age

The location of a star in the HR diagram does not allow for a unique age determination as several combinations of chemical composition ( $[M/H]$ ,  $[\alpha/Fe]$ ,  $Y$ , etc.) and age are possible (see e.g. Binney & Merrifield 1998). Individually, accurate ages require extremely accurate determinations of luminosity, temperature, reddening and chemical composition, which *Gaia* will provide.

For ages around 10–14 Gyr and assuming a given chemical composition, a change of  $\log T_{\text{eff}}$  by  $\sim 0.01$  dex for the stars in the turn-off translates to an age variation of 2 Gyr. Thus, temperatures must be known with precisions better than a few hundredths in  $\log T_{\text{eff}}$ , i.e. 1.5–2 per cent in  $T_{\text{eff}}$ , for the turn-off stars to determine individually accurate ages. A variation of 0.3 dex in  $[M/H]$  is equivalent to a change of  $\log T_{\text{eff}}$  by  $\sim 0.01$  dex for a given age. The variation of the  $\alpha$ -element abundance has a smaller impact on the age determination than the variation of  $[M/H]$ . A variation of  $+0.3$  dex in  $[\alpha/Fe]$  leads to a variation of  $-0.006$  dex in the temperature turn-off, yielding an uncertainty of about 1 Gyr in the age.

In summary, an uncertainty of about 4–5 Gyr is estimated for the individual ages of the stars at the turn-off for the halo, thick-disc and old-thin-disc stars up to about 2, 3 and 5 kpc in the Galactic centre, anticentre and orthogonal directions, respectively, as deduced from the PS performances in Section 7.

The age determination for F–G subgiant stars is quite insensitive to uncertainties in  $T_{\text{eff}}$  because the isochrones are almost horizontal. An uncertainty in  $M_V$  of about 0.15 translates to an uncertainty in the age of about 2 Gyr. Assuming additional uncertainties in  $[M/H]$  and  $[\alpha/Fe]$  determinations of about 0.3 dex, the final precision of the individual ages is about 3–4 Gyr.

Kučinskas et al. (2003) showed that early-AGB stars can provide ages as accurate as the turn-off stars for  $[M/H] > -1.5$  when  $\sigma_{\log T_{\text{eff}}} \sim 0.01$ ,  $\sigma_{\log g} \sim 0.2$ ,  $\sigma_{[M/H]} \sim 0.2$  and  $\sigma_{E_{B-V}} \sim 0.03$ , thus allowing the age determination to larger distances than for turn-off and subgiant stars. The *Gaia* capabilities in the case of metal-poor stars have not yet been investigated.

Subsets of each Galactic population (such as globular clusters, open clusters, OB associations, a given halo stream, an identified merger, a moving group, etc.) can be treated statistically and mean

ages and chemical abundances of the group can be obtained with much better precisions than those of the individual members.

The prospects for the determination of the age–metallicity relation and the star formation history with *Gaia* are discussed by Haywood (2005). Assuming the errors on the APs from Section 7, the author recovers the simulated age–metallicity relation in the case of moderate extinction and for a slowly varying SFR. The details of the star formation history, such as a series of prominent short bursts, are not recovered.

#### 8.5 Quasi-stellar objects

QSOs play an important role in the *Gaia* mission as they will be used to construct the astrometric reference frame and they are of course interesting in their own right. However, because the QSO population only represents 0.05 per cent of the stellar population, building a *secure* QSO sample with no stellar contamination requires a very efficient rejection algorithm. Although proper motion, parallax and variability information will help in rejecting stars, these will be available with the required precision only at the end of the mission. Therefore, it is important to check the capability to classify QSOs using only photometric data.

The QSO classification efficiencies of supervised NNs and of MDMs (see Section 7.2) have been compared using synthetic data generated from the BaSeL 2.2 library for stars (Lejeune et al. 1998), from pure-hydrogen atmosphere models for white dwarfs (Koester, private communication) and from a library of QSO synthetic spectra (Claeskens, Smette & Surdej 2005; Claeskens et al. 2006). Properly trained NNs are found to be capable of rejecting virtually *all* stars, including white dwarfs. This is at the expense of the completeness level of the QSO sample, being only  $\sim 20$  per cent at  $G = 20$ . However, this provides a sufficient number of objects in the context of the non-rotating extragalactic reference system determination. MDMs provide a higher completeness level ( $\sim 60$  per cent at  $G = 20$ ), but with a correspondingly higher stellar contamination rate of the QSO sample. MDMs may be preferred at high Galactic latitudes. Not surprisingly, reddened QSOs and weak emission-line objects are preferentially lost while high-redshift objects are most easily recognized.

Assuming an object is a QSO, it is also possible to infer its redshift from its photometric signature in the C1B+C1M passbands. Unfortunately, there is a colour degeneracy in the QSO spectra that limits the expected precision of the technique to about  $|\Delta z|_{\text{Median}} \simeq 0.2$  in the range  $0.5 < z_{\text{spec}} < 2$  (computations were done with a previous version of the *Gaia* PS but are not strongly sensitive to the adopted filter sets).

More details on the identification and characterization of QSOs with *Gaia* can be found in Claeskens et al. (2005).

## 9 CONCLUSIONS

To fully achieve the scientific goals of the *Gaia* mission, it is essential to complement the astrometric and radial velocity measurements with highly accurate multicolour photometry. This is necessary both for obtaining accurate astrometry and for a proper scientific interpretation of the stereoscopic census of the Galaxy *Gaia* will provide. The latter goal requires that the PS for *Gaia* is capable of astrophysically parametrizing 1 billion objects across the entire HR diagram in the presence of varying degrees of reddening and for the full range of chemical compositions and ages of stars populating the Galaxy and of identifying peculiar objects and QSOs.

There are no existing PSs capable of handling this very demanding task. We therefore set out to design a new system for the *Gaia* mission. The broad passbands implemented in the Astro instrument should fulfil the chromaticity requirements from the astrometric data processing, while at the same time allowing for the astrophysical characterization of stars in very crowded regions. The main classification and astrophysical parametrization task is carried out with the medium passbands implemented in the Spectro instrument.

The novel development we introduce in this work is the use of an objective FoM to compare different proposals for the *Gaia* PS. This FoM is based on the predicted errors that can be obtained for the parametrization of stars in terms of  $T_{\text{eff}}$ ,  $\log g$ ,  $A_V$ ,  $[M/H]$  and  $[\alpha/Fe]$ . These errors are calculated by using synthetic spectra to evaluate the sensitivity of each photometric passband to the APs. At the same time, the degree of local degeneracy in the APs is taken into account in the FoM. The overall FoM for a PS is calculated taking into account the priorities of the different STs that were deemed to be most important for addressing the core science case for *Gaia*. Using the FoM allows us to choose objectively which of the many proposed PSs is best in terms of reaching the APs error goals, while at the same time having the least number of local degeneracies.

The calculation of the predicted posterior errors and the FoM as outlined in Appendix A can be applied to any PS and can also be used to predict parametrization errors that can be achieved with spectra of stars. In addition, our method can be extended to the optimization of systems that can be used for the study of high-redshift galaxies or quasars (for example to derive photometric redshifts), as long as the dependence of the relevant SEDs on parameters such as redshift or SFR are known.

The main contribution of this work is the PS itself. This system has been designed based on our astrophysical knowledge and experience with ground-based systems and resulted in five (C1B) and 14 (C1M) passbands implemented in the Astro and Spectro instruments, respectively. The number of passbands reflects the variety of targets (all types of stars, QSOs, galaxies, Solar system objects), the required stellar APs ( $T_{\text{eff}}$ ,  $\log g$ ,  $A_V$ ,  $[M/H]$ ,  $[\alpha/Fe]$ ) and the need of breaking degeneracies (changes in two or more parameters may translate to the same changes in some spectral features but different changes in other ones). In summary, three of the broad C1B passbands are located to the left of  $H\beta$  line, on the  $H\alpha$  line and to the right of Paschen jump. The other two passbands fill the gaps so that full coverage of the whole spectral range of *Gaia* observations is provided. A broad passband in C1M, implemented in the Spectro instrument, provides the measurement of the UV flux at wavelengths bluewards of the Balmer jump. Seven medium passbands are placed on the crowding of Balmer series in early-type stars, on the Ca II H line, on the Mg I triplet and MgH band, on the  $H\alpha$  line, on one of TiO absorption bands in cool stars, and on the strong CN band in R- and N-type stars. An additional passband serves to measure the flux in the wavelength range covered by RVS. Finally, five passbands are devoted to the measurement of the pseudo-continuum.

The unfiltered light measured in the Astro and Spectro instruments provides photometric data in two very broad passbands (from 400 to 1000 nm and from 350 to 1025 nm). The  $G$  magnitude from Astro yields the highest S/N among all *Gaia* magnitudes and hence is the most suitable for variability analysis.

End-of-mission magnitude precisions have been estimated following an ‘aperture photometry’ approach. A precision of 0.01 mag is obtained at  $V \sim 18$  and 16 for the C1B and C1M passbands, respectively. In the case of the  $G$  passband and for stars brighter than  $V \sim 16$  and  $\sim 14$  measured with C1B and C1M, respectively, the photometric precision is limited by how accurately the data are

calibrated. Although there is no detailed calibration model, a rough estimation of the number of involved calibration parameters and the number of available stars for calibration purposes shows that sub-millimagnitude photometric precisions are potentially achievable. A PSF-fitting approach shows that it is possible to deal with stellar densities up to about  $2\text{--}4 \times 10^5$  stars  $\text{deg}^{-2}$  to 20 mag with Spectro, if accurate positional information from astrometry is used.

The performance of the *Gaia* PS with respect to the determination of APs for single stars has been evaluated using the ‘posterior’ errors from the FoM formalism and using algorithms designed for the astrophysical parametrization of stars (based on MDM and NN). The differences and limitations have been discussed. Both approaches demonstrate that precision goals in Section 4.3 are generally achieved to  $G \sim 17\text{--}18$  mag and that the precision for each parameter depends on temperature, luminosity, chemical composition and interstellar extinction, and apparent magnitude, as expected. Reasonable uncertainties of 0.5–1 dex are obtained even for the chemical composition of metal-poor stars ( $[M/H] = -4.0$ ). The determination of  $[\alpha/Fe]$  to a precision of about 0.1–0.2 dex is possible down to  $G \sim 16\text{--}17$  for low- to intermediate-temperature stars. Assuming a standard extinction law, the C1B and C1M passbands allow the determination of individual extinctions and, hence, the determination of  $T_{\text{eff}}$  is reliable, even in the presence of significant extinction, down to at least  $G = 18$ . By combining photometry and astrometry, a statistical approach to the construction of a 3D Galactic extinction map is also possible. *Gaia* will yield parallaxes with relative uncertainties lower than 10 per cent for some 100–200 million stars allowing absolute magnitude determinations across the entire HR diagram if the extinction is known. The C1B+C1M system is designed to provide the same luminosity errors (0.1–0.2 dex in  $\log g$ ) for giants and early-type stars at large distances, ensuring the study of the Galactic structure on large scales. Individual ages of stars at the turn-off of the halo and old-thin and thick disc at distances up to about 2, 3 and 5 kpc in the Galactic centre, anticentre and orthogonal directions, respectively, can be determined with a precision of about 4–5 Gyr. The same precisions can be obtained for early-AGB stars, thus allowing the probing of larger distances than with turn-off and subgiant stars. For subgiants, our estimations yield slightly lower uncertainties of 3–4 Gyr. Note that we quote uncertainties for individual ages. For a group of stars, the mean age will be determined to much better precision.

An additional merit of the *Gaia* PS is its ability to discriminate QSOs from stars and white dwarfs. This will result in a sufficient number of objects for the definition of the non-rotating extragalactic reference system for proper motions.

Finally, the performance of the C1B passbands when dealing with the chromaticity residuals has been evaluated. Our estimates show that the chromatic contribution to the parallax errors is 0.14–1.4  $\mu\text{s}$ . As these numbers are based on a worst-case assumption for the WFE and a somewhat simplistic calibration model, a residual contribution of 1  $\mu\text{s}$  for stars and of a few microarcsec for the QSOs is likely achievable.

In summary, the PS C1B+C1M developed by the Photometry Working Group satisfies the mission requirements and was therefore adopted as the baseline by the *Gaia* Science Team. It has since been adopted by the ESA Project Team as the basis for the formal mission requirements to the industrial teams participating in the ESA Invitation to Tender for *Gaia*.

The experience from the development of the PS, including selecting the STs and the ‘FoM’ approach, puts us in a good position to rapidly optimize new payload proposals that will come from the selected industrial contractor in the course of 2006.

## ACKNOWLEDGMENTS

We would like to acknowledge the contributions by B. Edvardsson, R. Lazauskaite, T. Lejeune and J. Sudzius and the collaborative effort of members of the Photometry Working Group within the *Gaia* mission preparation framework. We also thank P. Hauschildt, I. Brott and F. Castelli for making available to us SED libraries with  $\alpha$ -element enhanced abundances. The authors acknowledge the funding support from the following countries: Belgium, Denmark (through the Danish Ministry of Science), Estonia (through the ESF grants nos 5003 and 6106), France, Germany (through the DLR and the Emmy Noether Programme of the DFG), Greece (through GSRT), Italy, Lithuania (through the Ministry of Education and Science), the Netherlands (through the Netherlands Research School for Astronomy NOVA and the Netherlands Organisation for Scientific Research NWO), Russia, Spain (through MCYT under contract PNE2003-04352), Sweden, Switzerland and the United Kingdom. For Denmark, Estonia, Lithuania and Sweden, support from the Nordic Research Board (ref. NB00-N030 and 2001-2783-4) is gratefully acknowledged. AK acknowledges the Wenner-Gren Fellowship. Finally, we would like to thank the referee, M.S. Bessell, for a rapid response and constructive comments that helped improve the paper.

## REFERENCES

- Arenou F., Babusiaux C., Chéreau F., Mignot S., 2005, in Perryman M. A. C., Turon C., O’Flaherty K. S., eds, Proc. Symp. ESA SP-576, The Three Dimensional Universe with Gaia. ESA Publications Division, Noordwijk, p. 335
- Bailer-Jones C. A. L., 1998, Technical report, Statnet. Available at <http://www.mpia.de/homes/calj/statnet.html>
- Bailer-Jones C. A. L., 2000, *A&A* 357, 197
- Bailer-Jones C. A. L., 2003, in Munari U., ed., ASP Conf. Ser. Vol. 298, GAIA Spectroscopy, Science and Technology. Astron. Soc. Pac., San Francisco, p. 199
- Bailer-Jones C. A. L., 2004, *A&A*, 419, 385
- Bailer-Jones C. A. L., 2005, in Perryman M. A. C., Turon C., O’Flaherty K. S., eds, Proc. Symp. ESA SP-576, The Three Dimensional Universe with Gaia, ESA Publications Division, Noordwijk, p. 393
- Bessell M. S., 2005, *ARA&A*, 43, 293
- Bessell M. S., Brett J. M., Scholtz M., Wood P. R., 1989, *A&AS*, 77, 1
- Bessell M. S., Castelli F., Plez B., 1998, *A&A*, 333, 231 (erratum 337, 321)
- Binney J., Merrifield M., 1998, *Galactic Astronomy*. Princeton Univ. Press Princeton
- Bridžius A., Vanevičius V., 2002, *Ap&SS*, 280, 41
- Brott I., Hauschildt P. H., 2005, in Perryman M. A. C., Turon C., O’Flaherty K. S., eds, Proc. Symp. ESA SP-576, The Three Dimensional Universe with Gaia, ESA Publications Division, Noordwijk, p. 393
- Brown A. G. A., 2003, Results of the Second Cycle of Blind Testing, Gaia technical report ICAP-AB-004. <http://gaia.am.ub.es/PWG/documents/MNRAS>
- Brown A. G. A., 2005, in Perryman M. A. C., Turon C., O’Flaherty K. S., eds, Proc. Symp. ESA SP-576, The Three Dimensional Universe with Gaia, ESA Publications Division, Noordwijk, p. 377
- Brown A. G. A., Jordi C., Knude J., Høg E., 2004, Procedure for Photometric Systems Recommendation, Gaia technical report PWG-AB-003. <http://gaia.am.ub.es/PWG/documents/MNRAS>
- Cardelli J. A., Clayton G. C., Mathis J. S., 1989, *ApJ*, 345, 245
- Cayrel de Strobel G., Soubiran C., Ralite N., 2001, *A&A*, 373, 159
- Cellino A., Delbò M., Dell’Oro A., Zappalà V., 2005, in Perryman M. A. C., Turon C., O’Flaherty K. S., eds, Proc. Symp. ESA SP-576, The Three Dimensional Universe with Gaia, ESA Publications Division, Noordwijk, p. 231
- Claeskens J.-F., Smette A., Surdej J., 2005, in Perryman M. A. C., Turon C., O’Flaherty K. S., eds, Proc. Symp. ESA SP-576, The Three Dimensional Universe with Gaia, ESA Publications Division, Noordwijk, p. 667
- Claeskens J.-F., Smette A., Vandenberg L., Surdej J., 2006, *MNRAS*, in press (doi: 10.1111/j.1365-2966.2006.10024.x)
- Dollet C., Bijaoui A., Mignard F., 2005, in Perryman M. A. C., Turon C., O’Flaherty K. S., eds, Proc. Symp. ESA SP-576, The Three Dimensional Universe with Gaia, ESA Publications Division, Noordwijk, p. 429
- Drimmel R., Cabrera-Lavers A., López-Corredoira M., 2003, *A&A*, 409, 205
- Drimmel R., Bucciarelli B., Lattanzi M. G., Spagna A., Jordi C., Robin A. C., Reylé C., Luri X., 2005, in Perryman M. A. C., Turon C., O’Flaherty K. S., eds, Proc. Symp. ESA SP-576, The Three Dimensional Universe with Gaia, ESA Publications Division, Noordwijk, p. 163
- ESA-SCI(2000)4, 2000, GAIA: Composition, Formation and Evolution of the Galaxy.
- Evans D. W., 2004, MBP Profile Fitting in Crowded Regions, Gaia technical report PWG-DWE-001. <http://gaia.am.ub.es/PWG/documents/MNRAS>
- Eyer L., 2005, in Perryman M. A. C., Turon C., O’Flaherty K. S., eds, Proc. Symp. ESA SP-576, The Three Dimensional Universe with Gaia, ESA Publications Division, Noordwijk, p. 513
- Eyer L., Mignard F., 2005, *MNRAS*, 361, 1136
- Fiorucci M., Munari U., 2003, *A&A*, 401, 781
- Fitzpatrick E. L., 1999, *PASP*, 111, 63
- Fluks M. A., Plez B., Thé P. S., de Winter D., Westerlund B. E., Steenman H. C., 1994, *A&AS*, 105, 311
- Grenon M., Jordi C., Figueras F., Torra J., 1999, An intermediate Band System for GAIA, Gaia technical report MGUB-PWG-002. <http://gaia.am.ub.es/PWG/documents/MNRAS>
- Gunn F. E., Stryker L. L., 1983, *ApJS*, 52, 121
- Gustafsson B., Edvardsson B., Eriksson K., Jørgensen U. G., Mizuno-Wiedner M., Plez B., 2003, in Piskunov N., Weiss W. W., Gray D. F., eds, Proc. IAU Symp. 210, Modelling of Stellar Atmospheres. Kluwer, Dordrecht, p. A4
- Haywood M., 2005, in Perryman M. A. C., Turon C., O’Flaherty K. S., eds, Proc. Symp. ESA SP-576, The Three Dimensional Universe with Gaia, ESA Publications Division, Noordwijk, p. 521
- Hastie T., Tibshirani R., Friedman J., 2001, *The Elements of Statistical Learning*. Springer-Verlag, New York
- Hauschildt P. H., Allard F., Baron E., 1999, *ApJ*, 512, 377
- Hauschildt P. H., Allard F., Baron E., Aufdenberg J., Schweitzer A., 2003, in Munari U., ed., ASP Conf. Ser. Vol. 298, GAIA Spectroscopy, Science and Technology. Astron. Soc. Pac., San Francisco, p. 179
- Heiter U., Piskunov N., Gustafsson B., Jordi C., Carrasco J. M., 2005, in Favata F., Hussain G., Battrick B., eds, ESA SP-560, Proc. 13th Cambridge Workshop on Cool Stars, Stellar Systems and the Sun. ESA Publications Division, Noordwijk, p. 635
- Høg E., 1993, in Mueller I. I., Kolaczek B., eds, IAU Symp. 156, Developments in Astrometry and their Impacts on Astrophysics and Geodynamics. Kluwer, Dordrecht, p. 37
- Høg E., 1998, Spectrophotometry or Filter Photometry for Gaia?, Gaia technical report SAG-CUO-045. <http://gaia.am.ub.es/PWG/documents/MNRAS>
- Høg E., 2005, Summary of Sampling Schemes for ASM, AF, BBP, SSM and MBP, Gaia technical report GAIA-CUO-151V3. <http://gaia.am.ub.es/PWG/documents/MNRAS>
- Høg E., Knude J., 2004a, Two New MBP Systems: K2M and K3M, Gaia technical report GAIA-CUO-152. <http://gaia.am.ub.es/PWG/documents/MNRAS>
- Høg E., Knude J., 2004b, Four New MBP Systems: K4M, K5M, K6M, K7M, Gaia technical report GAIA-CUO-155. <http://gaia.am.ub.es/PWG/documents/MNRAS>
- Jordi C., Carrasco J. M., 2004a, BBP Systems Proposals, Gaia technical report UB-PWG-026. <http://gaia.am.ub.es/PWG/documents/MNRAS>
- Jordi C., Carrasco J. M., 2004b, MBP Systems Proposals, Gaia technical report UB-PWG-027. <http://gaia.am.ub.es/PWG/documents/MNRAS>

- Jordi C., Grenon M., Figueras F., Torra J., Carrasco J. M., 2003, The 2F Geneva-Barcelona Medium Band Photometric System for GAIA, Gaia technical report UB-PWG-011. <http://gaia.am.ub.es/PWG/documents/MNRAS>
- Jordi C., Carrasco J. M., Høg E., Brown A. G. A., Knude J., 2004a, BBP Photometric Systems Evaluation, Gaia technical report UB-PWG-028. <http://gaia.am.ub.es/PWG/documents/MNRAS>
- Jordi C., Carrasco J. M., Høg E., Brown A. G. A., Knude J., 2004b, BBP Photometric Systems Evaluation, Gaia technical report UB-PWG-029. <http://gaia.am.ub.es/PWG/documents/MNRAS>
- Jordi C., Figueras F., Torra J., Carrasco J. M., 2004c, The 3F Geneva-Barcelona Medium Band Photometric System for Gaia, UB-PWG-016. <http://gaia.am.ub.es/PWG/documents/MNRAS>
- Jordi C., Figueras F., Carrasco J. M., Knude J., 2004d, Gaia Scientific Targets for PS Design, Gaia technical report UB-PWG-009v1.1. <http://gaia.am.ub.es/PWG/documents/MNRAS>
- Jordi C., Knude J., Carrasco J. M., Figueras F., 2004e, Gaia Scientific Targets for PS Design: Quantification of Priorities, Gaia technical report UB-PWG-015v1.2. <http://gaia.am.ub.es/PWG/documents/MNRAS>
- Kaempf T. A., Willemsen P. G., Bailer-Jones C. A. L., 2005, in Perryman M. A. C., Turon C., O'Flaherty K. S., eds, Proc. Symp. ESA SP-576, The Three Dimensional Universe with Gaia, ESA Publications Division, Noordwijk, p. 441
- Kalcheva N., Knude J., Georgiev V., 2003, A&A, 407, 377
- Katz D., Soubiran C., Cayrel R., Adda M., Cautain R., 1998, A&A, 338, 151
- Katz D. et al., 2004, MNRAS, 354, 1223
- Knude J., 2002, Ap&SS, 280, 97
- Knude J., Fabricius C., 2003, Baltic Astron., 12, 508
- Knude J., Høg E., 2004, A New MBP System: K1M, Gaia technical report GAIA-CUO-148. <http://gaia.am.ub.es/PWG/documents/MNRAS>
- Kolka I., Eelmäe T., Hirv A., Tuvikene T., Kama M., 2005, in Perryman M. A. C., Turon C., O'Flaherty K. S., eds, Proc. Symp. ESA SP-576, The Three Dimensional Universe with Gaia, ESA Publications Division, Noordwijk, p. 543
- Kučinskas A., Lindegren L., Tanabé T., Vasevičius V., 2003, in Munari U., ed., ASP Conf. Ser., Vol. 298, GAIA Spectroscopy, Science and Technology. Astron. Soc. Pac., San Francisco, p. 415
- Kučinskas A., Hauschildt P. H., Ludwig H.-G., Brott I., Vasevičius V., Lindegren L., Tanabé T., Allard F., 2005, A&A, 442, 281
- Kurucz R. L., 1979, ApJS, 40, 1
- Lejeune T., Cuisinier F., Buser R., 1998, A&AS, 130, 65
- Lindegren L., 2001, GAIA Chromaticity Calibration and Design of the Broad Band Photometry System, Gaia technical report GAIA-LL-039. <http://gaia.am.ub.es/PWG/documents/MNRAS>
- Lindegren L., 2003a, Photometric Systems for Gaia's Broad Band Photometer, Gaia technical report GAIA-LL-045. <http://gaia.am.ub.es/PWG/documents/MNRAS>
- Lindegren L., 2003b, Optimizing Gaia's Photometric System: Thoughts on Distance Measure and Figure of Merit, Gaia technical report GAIA-LL-047. <http://gaia.am.ub.es/PWG/documents/MNRAS>
- Lindegren L., 2003c, Gaia Chromaticity Calibration and the BBP Filter Shape, Gaia technical report GAIA-LL-049. <http://gaia.am.ub.es/PWG/documents/MNRAS>
- Lindegren L., 2004, Use of Parallax Information in the Photometric System Design, Gaia technical report GAIA-LL-054. <http://gaia.am.ub.es/PWG/documents/MNRAS>
- Maeder A., 1999, in Noels A., Magain P., Caro D., Jehin E., Parmentier G., Thoul A.A., eds, Proc. 35th Liege Internat. Astroph. Colloq., The Galactic Halo: From Globular Clusters to Field Stars. University of Liège, Liège, p. 1
- Malyuto V., 2005, in Perryman M. A. C., Turon C., O'Flaherty K. S., eds, Proc. Symp. ESA SP-576, The Three Dimensional Universe with Gaia, ESA Publications Division, Noordwijk, p. 453
- Mégessier C., 1995, A&A, 296, 771
- Mignard F., 2005, in Perryman M. A. C., Turon C., O'Flaherty K. S., eds, Proc. Symp. ESA SP-576, The Three Dimensional Universe with Gaia, ESA Publications Division, Noordwijk, p. 5
- Moro D., Munari U., 2000, A&AS, 147, 361
- Munari U., 1999, Baltic Astron., 8, 123
- Munari U., Sordo R., Castelli F., Zwitter T., 2005, A&A, 442, 1127
- Nissen P. E., 1999, in Noels A., Magain P., Caro D., Jehin E., Parmentier G., Thoul A. A., eds, Proceedings of The Galactic halo: From Globular Clusters to Field Stars, Université de Liège, p. 125
- Nurmi P., 2005, Ap&SS, 298, 559
- Perryman M. A. C. et al., 2001, A&A, 369, 339
- Pickles A. J., 1998, PASP, 110, 863
- Press W. H., Teukolsky S. A., Vetterling W. T., Flannery B. P., 1992, Numerical Recipes in Fortran: The Art of Scientific Computing, 2nd edn. Cambridge Univ. Press, Cambridge
- Robin A. C., Reylé C., Derrière S., Picaud S., 2003, A&A, 409, 523
- Robin A. C., Reylé C., Picaud S., Schultheis M., 2005, A&A, 430, 129
- Straizys V., 1992, Multicolor Stellar Photometry. Pachart Publishing House, Tucson
- Straizys V., 2004, A Revised Version of the BBP System for Gaia: V1B, Gaia technical report GAIA-VILN-002. <http://gaia.am.ub.es/PWG/documents/MNRAS>
- Straizys V., Høg E., 1995, in Perryman M. A. C., van Leeuwen G., eds, ESA SP-379, Future Possibilities for Astrometry in Space. ESA Publications Division, Noordwijk, p. 191
- Straizys V., Høg E., Vasevičius V., 2000, The 3G Photometric System, Gaia technical report SAG-CUO-78. <http://gaia.am.ub.es/PWG/documents/MNRAS>
- Straizys V., Zdanavičius K., Lazauskaitė R., 2004, A New Version of the MBP System for Gaia: V2M, Gaia technical report GAIA-VILN-001. <http://gaia.am.ub.es/PWG/documents/MNRAS>
- Tautvaišienė G., Edvardsson B., 2002, Ap&SS, 280, 143
- Tautvaišienė G., Edvardsson B., 2005, in Perryman M. A. C., Turon C., O'Flaherty K. S., eds, Proc. Symp. ESA SP-576, The Three Dimensional Universe with Gaia, ESA Publications Division, Noordwijk, p. 549
- Tautvaišienė G., Edvardsson B., Bartašūtė S., 2003, Baltic Astron., 12, 532
- Torra J., Chen B., Figueras F., Jordi C., Luri X., 1999, Baltic Astron., 8, 171
- Vasevičius V., Bridžius A., 2002, Gaia Photometric Performances, Gaia technical report GAIA-VIL-008. <http://gaia.am.ub.es/PWG/documents/MNRAS>
- Vasevičius V., Bridžius A., 2003, in Munari U., ed., ASP Conf. Ser. Vol. 298, GAIA Spectroscopy, Science and Technology. Astron. Soc. Pac., San Francisco, p. 41
- Wahlgren G. M., Lundqvist M., Kučinskas A., 2005, in Perryman M. A. C., Turon C., O'Flaherty K. S., eds, Proc. Symp. ESA SP-576, The Three Dimensional Universe with Gaia, ESA Publications Division, Noordwijk, p. 619
- Wilkinson M. I. et al., 2005, MNRAS, 359, 1306
- Willemsen P. G., Bailer-Jones C. A. L., 2005, Determination of  $\alpha$ -Abundances from Gaia Photometric Data, Gaia technical report ICAP-PW-008. <http://gaia.am.ub.es/PWG/documents/MNRAS>
- Willemsen P. G., Kaempf T. A., Bailer-Jones C. A. L., 2005a, Neural Network Parametrization Performances for the C1M and C1B Photometric Systems, Gaia technical report ICAP-PW-006. <http://gaia.am.ub.es/PWG/documents/MNRAS>
- Willemsen P. G., Kaempf T. A., de Boer K. S., Bailer-Jones C. A. L., 2005b, Using Distance Information in the Process of Automated Parametrization – Preliminary Results, Gaia technical report ICAP-PW-005. <http://gaia.am.ub.es/PWG/documents/MNRAS>

## APPENDIX A: FIGURE OF MERIT

The definition and the procedure for calculating an FoM for a PS was proposed by Lindegren (2003b) and we provide the details here.

The achievable errors  $\sigma_{ik, \text{post}}$  for a particular ST  $i$  can be calculated using the so-called sensitivity matrix  $\mathbf{S}_i$ . The elements of this matrix are the partial derivatives  $\partial\phi_{ij}/\partial p_k$ , where  $\phi_{ij}$  is the (noise-free) normalized flux in filter  $j$  (in photon counts) for ST  $i$ , and  $p_k$  stands for the AP  $k$ . These derivatives describe how the flux in each



filter changes in response to a change in AP  $k$ . Consider the AP determination as a linearized least-squares estimation of  $\Delta \mathbf{p}$ , the improvement of the AP vector. The observation equation for ST  $i$  resulting from the flux measured in filter  $j$  reads

$$\frac{\partial \phi_{ij}}{\partial p_1} \Delta p_1 + \dots + \frac{\partial \phi_{ij}}{\partial p_K} \Delta p_K = \Delta \phi_{ij} \pm \epsilon_{ij}, \quad (\text{A1})$$

where  $\Delta \phi_{ij} = \phi_{ij,\text{obs}} - \phi_{ij}(\mathbf{p})$  is the difference between the observed and predicted flux and  $\epsilon_{ij}$  indicates the flux uncertainty. Observation equations of unit weight are formed through division by  $\epsilon_{ij}$ , whereupon normal equations are formed in the usual manner. The linearization is assumed to be made around the true parameter vector  $\mathbf{p}$ , so that the resulting update  $\Delta \mathbf{p}$  has zero expectation. Then, given the variance–covariance matrix  $\mathbf{C}_\phi = \text{diag}(\epsilon_{ij}^2)$  of the observed fluxes, the variance–covariance matrix of the estimated AP vector  $\mathbf{p}_{\text{post}}$  is given by the inverse of the normal equations matrix:

$$\mathbf{C}_{\mathbf{p},\text{post}} = (\mathbf{S}^T \mathbf{C}_\phi^{-1} \mathbf{S})^{-1}, \quad (\text{A2})$$

where the matrices  $\mathbf{C}_{\mathbf{p},\text{post}}$ ,  $\mathbf{C}_\phi$  and  $\mathbf{S}$  are defined for each ST  $i$  separately. The diagonal elements  $[\mathbf{C}_{\mathbf{p},\text{post}}]_{kk} = \sigma_{ik,\text{post}}$  of this matrix are the sought after achievable errors for a PS. In reality, degeneracy among the APs will often make the matrix  $(\mathbf{S}^T \mathbf{C}_\phi^{-1} \mathbf{S})^{-1}$  singular or near-singular, resulting in infinite or very large  $\sigma_{ik,\text{post}}$  as computed from equation (A2). This can be avoided by adding a suitable positive definite matrix  $\mathbf{B}$ , which makes the whole right-hand side positive definite; thus,

$$\mathbf{C}_{\mathbf{p},\text{post}} = (\mathbf{B} + \mathbf{S}^T \mathbf{C}_\phi^{-1} \mathbf{S})^{-1}. \quad (\text{A3})$$

$\mathbf{B}$  is the a priori information matrix of the APs. In the absence of any other information on the APs we have  $\mathbf{B} = \text{diag}(\sigma_{ik,\text{prior}}^{-2})$ . This matrix plays an important role and can be used to incorporate prior information on the APs. This matrix can also be used to incorporate constraining information from the parallax measurements. When the photometric data do not provide any relevant information on a given AP  $p_k$  (either because the flux variances in  $\mathbf{C}_\phi$  are too large or because the elements of the sensitivity matrix  $\mathbf{S}$  are too small), then  $\sigma_{ik,\text{post}} \simeq \sigma_{ik,\text{prior}}$ .

In practice, the derivatives  $\partial \phi_{ij} / \partial p_k$  are calculated numerically from simulated photometric data. The calculation thereof requires (synthetic) SEDs of the STs and a noise model for the photometric instruments.

The FoM is now calculated as follows. For each ST  $i$  and AP  $k$  ( $A_V$ ,  $[M/H]$ ,  $\log g$ ,  $T_{\text{eff}}$ ,  $[\alpha/\text{Fe}]$ , ...) the performance of the PS is measured by the ratio  $\sigma_{ik,\text{post}} / \sigma_{ik,\text{goal}}$ . The FoM  $Q_i$  for each ST  $i$  is then defined as

$$Q_i = \sum_k w_k f(\sigma_{ik,\text{post}} / \sigma_{ik,\text{goal}}), \quad (\text{A4})$$

where  $w_k$  indicates the relative weight of each AP (with  $\sum_k w_k = 1$ ) and  $f(x)$  is a non-linear function of  $x = \sigma_{ik,\text{post}} / \sigma_{ik,\text{goal}}$  with a break around 1. The function used is

$$f(x) = (1 + x^{2n})^{-1/n}. \quad (\text{A5})$$

The global FoM (summed over all STs) is the weighted and normalized sum:

$$\widehat{Q} = \frac{\sum_i w_i Q_i}{\sum_i w_i}, \quad (\text{A6})$$

where the weights  $w_i$  indicate the priority of each ST  $i$ . The value of  $\widehat{Q}$  indicates how close the performance of a PS is to being ‘ideal’ (when  $\widehat{Q} = 1$ ). This global FoM is then calculated for each PS using the error goals, weights and priorities defined in Jordi et al. (2004e).

The value of  $n$  in the function  $f(x)$  from equation (A5) determines how much weight good performance ( $x \leq 1$ ) gets in the FoM as opposed to bad performance ( $x > 1$ ). We are looking for a PS that achieves the error goals over all of AP space and we want to avoid giving a high rank to a system that is extremely good in only one corner of AP space but very bad everywhere else. The latter will be highly ranked for  $n = 1$  but not for large  $n$ . However, for very large  $n$  (for which  $f(x)$  approaches a step function with  $f(x) = 0$  for  $x > 1$ ), we will not be able to tell the difference between two PSs that have the same amount of STs for which  $x > 1$  and  $x < 1$ , even though one of the two may be preferred because it reaches smaller values of  $x$  when  $x < 1$ . We chose the value of  $n = 3$  as a good compromise between these two extremes.

We end with a few remarks about the sensitivity matrix. The columns of  $\mathbf{S}_i$  are the gradient vectors that describe the changes of the fluxes with respect to a change in an AP. Thus,  $\mathbf{S}_i$  contains all the information needed to characterize the behaviour of the PS in the data space (or filter flux space) near ST  $i$ . In the ideal case, the gradient vectors would be aligned with the coordinate axes of the data space. That is each flux measurement  $\phi_{ij}$  is sensitive to one (and only one) AP. In practice, the gradient vectors are of course not aligned with the coordinate axes, which means that each AP influences some linear combination of fluxes. This also means that, even if all the gradient vectors are orthogonal, the errors in the APs will still be correlated, because any error on a measured flux  $\phi_{ij}$  will influence multiple AP determinations. These correlations are correctly taken into account in the calculation of the variance–covariance matrix of the estimated AP vector and are reflected in non-zero off-diagonal elements in this matrix.

A further complication that will occur in practice is that the gradient vectors will not be orthogonal to each other. This means that there will be degeneracies between the APs when we try to estimate them. A well-known example is the degeneracy between  $T_{\text{eff}}$  and  $A_V$  if only the continuum of the spectrum is measured. The behaviour of the PS depends on the noise and we should in fact consider the noise-weighted gradient vectors which have components  $1/\epsilon_{ij} \times \partial \phi_{ij} / \partial p_k$ . When the orthogonality is defined with respect to the noise-weighted gradient vectors, non-orthogonal gradient vectors will lead to larger correlations between the errors in the estimated APs and they will also cause the standard errors on each AP to increase. Without going into the mathematical detail, this can be appreciated if one considers that any degeneracy between two APs will make it more difficult to attribute flux changes to either of them, thus increasing the uncertainty in both parameters.

This means that a PS that contains larger degeneracies will get a lower FoM because of the increased  $\sigma_{ik,\text{post}}$  for degenerate APs. Note, however, that the FoM used in this sense is a measure of how good a particular PS is at *locally* separating stars with different APs along orthogonal directions. The FoM does not take *global* degeneracies into account, where very different parts of AP space are mapped onto each other in filter flux space.

This paper has been typeset from a  $\text{\TeX}/\text{\LaTeX}$  file prepared by the author.